Ellipticals with Kinematically-Distinct Cores: $V-I$ Color Images with WFPC2[1]

C. Marcella Carollo[2]

The Johns Hopkins University, Bloomberg Center, 21218 MD, Baltimore;

marci@pha.jhu.edu

Marijn Franx

Kapteyn Laboratory, University of Groningen, P.O. Box 800, 9700 AV Groningen, The Netherlands; franx@astro.rug.nl

Garth D. Illingworth and Duncan A. Forbes

Lick Observatory, University of California, Santa Cruz, CA 95064;

gdi@ucolick.org, forbes@ucolick.org

[1] Based on observations with the NASA/ESA Hubble Space Telescope, obtained at the Space Telescope Science Institute, which is operated by Association of Universities for Research in Astronomy, Inc. (AURA), under NASA contract NAS5-26555.

[2] Hubble Fellow

Received ____________________; accepted ____________________

ABSTRACT

We have analysed HST `WFPC2` F555W and F814W (i.e., V and I) images for fifteen elliptical galaxies with kinematically-distinct cores. For each of them we have derived surface brightness and isophotal parameter profiles in the two bands, color maps, and radial profiles in $V-I$. Most galaxies show patchy dust absorption close to their nuclei. However, there are generally no indications of homogeneous, diffuse dust components close to the nuclei. The nuclear colors in the unobscured regions are most likely representative of the central stellar populations.

We have detected photometric evidence for faint stellar disks, on scales of a few tens to a few arcseconds, in seven galaxies, namely NGC 1427, 1439, 1700, 4365, 4406, 4494 and 5322. In NGC 1700, the isophotes are slightly boxy at the scale of the counter-rotating component, and disky at larger radii. We find no difference in $V-I$ color greater than 0.02 mag between these disks and the surrounding galactic regions. Hence the stellar populations in the kinematically distinct cores are not strongly deviant from the population of the main body. Specifically, there is no evidence for a dominating population of blue, very metal weak stars, as predicted by some of the formation scenarios. This argues against models in which small galaxies fall in and survive in the nuclei, unless super massive black holes are present. These would in fact disrupt the accreted small systems.

For one galaxy, NGC 4365, the innermost region is bluer than the surrounding regions. This area extends to $\sim$ 15pc, and contains a luminosity of $\sim 2.5 \times 10^6$ $L_\odot$. If interpreted as a stellar population effect, an age difference of $\sim$ 3-4 Gyrs, or an $[Fe/H]$ variation of about 0.2 dex, is derived.

The nuclear intensity profiles show a large variety: some galaxies have steep

cusp profiles, others have shallow cusps and a "break radius". The nuclear cusps of galaxies with kinematically-distinct cores follow the same trends as the nuclei of normal galaxies.

We have not been able to identify a unique, qualifying feature in the `WFPC2` images which distinguish the galaxies with kinematically distinct cores from the kinematically normal cores. It is possible that statistical differences exist: possibly, the kinematically distinct cores have a higher fraction of nuclear disks. The similarity of both types of cores puts strong constraints on the formation scenarios. Simulations of galaxy mergers, with the inclusion of star formation and nuclear black holes, are needed to resolve the question how these structures may have formed. Spectra with high spatial resolution are needed to study the nuclear structure of the distinct component in detail.

1. Introduction

The study of nearby (kinematically-normal) elliptical galaxies performed with the `WF/PC` camera aboard the *Hubble Space Telescope* (HST) has revealed the presence of central disks, dust clouds, and nuclear components on scale lengths of a few tens of parsecs (e.g., Jaffe et al. 1994; van den Bosch et al. 1994; Lauer et al. 1995, hereafter L95; van Dokkum & Franx 1995). In all galaxies, the surface brightness profile $I(r)$ for $r \to 0.1''$ can be approximated as a power–law $r^{-\gamma}$, with $0 \lesssim \gamma \lesssim 1$. Galaxies with steep cusps are almost always small, fast–rotating objects, while in contrast massive, pressure–supported ones have shallow cusps, typically with $\gamma \lesssim 0.5$ (e.g., L95; Kormendy et al. 1995, hereafter K95). It is not clear whether this reflects a real dichotomy in the physical properties and formation processes, as suggested by L95 and K95. In any case, nuclear properties on scales of a few tens of parsecs are correlated with properties observed on global scales, and it is legitimate to ask whether this is the outcome of selection effects acting at formation, or whether it has resulted from subsequent galactic evolution.

Galaxies with kinematically-distinct cores are very interesting physical laboratories to test ideas of galaxy formation and evolution. Their distinct angular momenta suggest that these cores may be the relics of interactions or mergers, and thus may provide a powerful diagnostic to estimate the relevance of interactions in shaping galactic properties. Kormendy (1984) argued that the core of NGC 5813 is dominated by the remnant of a small galaxy that fell into a big elliptical. This scenario predicts core/global differences that should be detectable not only in the kinematics, but also in the stellar populations and overall structure. Another possible scenario for kinematically-distinct cores implies gas-rich mergers of two galaxies, where the gas is converted into stars in the central regions, and subsequent star formation produces a disk which retains the orbital signature of the original gas. Still another possibility is that formation of kinematically-distinct cores is a rather

normal aspect of a hierarchical formation scenario for elliptical galaxies, where galaxies are built up from pre-existing clumps (possibly different from current galaxies). The last two scenarios do not necessarily predict any measurable difference in the stellar population of the distinct core.

Forbes, Franx & Illingworth (1995, hereafter F95) investigated HST `WF/PC` F555W images for eight early-type galaxies with kinematically-distinct cores. These authors found clear indications of small-scale dust in six out of the eight galaxies, and argued that the dust might be directly linked to the existence of nuclear radio activity in these galaxies. They also showed that the nuclear surface brightness profiles in this class of galaxies are similar to those in kinematically-normal galaxies. On this basis, they argued against the plausibility of the small galaxy accretion scenario, since this low-mass object should dominate the light in the core region and produce differences with respect to normal galaxies (that are not observed). F95 searched for the nuclear disks expected in the dissipative core formation scenario (and suggested by spectroscopic analysis of several distinct cores, see e.g., Franx & Illingworth 1988). The search lead to one detection in NGC 4365 (previously reported by Forbes 1994), and to a couple of other candidates. In the other galaxies, no conclusions could be drawn due to the strong dust absorption.

Additional information is clearly needed to resolve the enigma of the formation of kinematically-distinct cores. Multi-color, high-resolution imaging can provide a valuable key for understanding the origin of these peculiar stellar systems. In particular, within the limits imposed by their degeneracy between age and metallicity, *(i)* color gradients between the core region and the rest of the galaxy could be used to estimate metallicity/age differences in the stellar populations; *(ii)* color information could help to detect nuclear disks, and indicate whether such disks were formed at the same time as the majority of stars (or more recently, as a bluer color might indicate); *(iii)* colors of the central cusps

could provide insight into their formation, discriminating between accretion of low-mass stellar systems (possibly leading to bluer cusps) and stars formed in situ (possibly leading to red cusps).

Observationally, colors and color gradients at subarcsecond scales are practically unexplored for any kind of galaxy. The only other example to date is that of Crane et al. (1993), who measured gradients for 12 galaxies using pre-refurbishment FOC data, and concluded that color variations are either very small or absent in galactic nuclei. However, these measurements are limited by low S/N and the uncertain `pre-COSTAR` PSF.

In this paper we extend the investigation started by F95 by studing `WFPC2` images in two bands, namely F555W and F814W (i.e., similar to Johnson V and Cousins I, respectively), for 15 galaxies with kinematically-distinct cores. The new sample contains the eight galaxies of F95, plus seven additional galaxies that also show peculiar core kinematics. Eleven of the galaxies are luminous objects with absolute V mag $M_V \leq$-20 + 5 log h ($h = H_o/100$ km s^{-1} Mpc^{-1} throughout this paper). The sample, the observations and the basic photometric analysis are described in Section 2. The V and I surface brightness profiles and the parameters defining the core morphology are presented in Section 3, together with the $V - I$ color profiles, the color maps, and the color gradients. In Section 4 we present the adopted parametrization of the surface brightness profiles, and derive the global estimator of the nuclear cusp-steepness which we will use in our discussion. In Section 5 we discuss the main results of this study, and summarize them in (the concluding) Section 6. In four appendices, we describe *(i)* the procedure used to minimize the effects of nuclear patchy dust on the derivation of the surface brightness profiles, *(ii)* the comparison of our `WFPC2` measurements with `WF/PC` profiles already published for some galaxies of our sample; *(iii)* the deprojections of the surface density profiles, performed in order to obtain an estimate of the physical luminosity density and of its nuclear radial variation; and *(iv)*

the derivation of the nuclear properties of the L95 galaxies, performed so as to compare kinematically-peculiar with normal galaxies. The properties of the globular cluster systems in our sample are derived and discussed by Forbes et al. (1996).

2. Observations and Measurements

2.1. The Sample

The 15 galaxies constituting the sample are listed in Table 1, together with some global parameters. The galaxies cover a large range in optical, infrared, X-ray and radio luminosities, and in metallicities (as characterized by central Mg_2 index values). Seven of them (NGC 1700, 3608, 4278, 4589, 5322, 5982 and 7626) belong to the sample of Schweizer et al. (1990), and cover a large range in the "fine-structure" Σ parameter (from a value of 3.7 for NGC 1700, to zero for NGC 3608 and NGC 4589). The environment of the galaxies varies considerably, with some galaxies closely paired to a companion in a rather loose group (e.g., IC 1459 and NGC 7626), and others embedded in rich clusters (e.g., the Virgo galaxy NGC 4406).

2.2. Data Reduction

For each galaxy we acquired two F555W exposures of 500 seconds each, and two F814W exposures of 230 seconds each. The observations were taken with the WFPC2 camera centered on PC1, with its scale of $0.046''$ px^{-1}, and a field of about $36'' \times 36''$.

Initial data reduction was performed using the standard STScI pipeline software. For each filter, the two available images were compared to each other, and found to have the

same central pixel value within Poisson statistics. Their relative alignment was checked before combining them, and found to be better than about 0.2 px. The two images were averaged and cosmic-ray cleaned using the cosmic ray rejection option of the STSDAS task "combine" , in combination with a noise model appropriate for the PC1 (all the images were taken with gain 15, except those for NGC 1439, 4406, 4552 and 5322, which were taken with gain 7). Hot and cold pixels were partly removed as well by the combining task; an interpolation over the remaining defects was subsequently performed. The cosmic-ray and bad-pixel removal was checked by inspecting the residual difference between the cleaned image and each of the two original frames. Except for NGC 1700, the observations were taken after 1994 April 24. We did not correct for charge transfer efficiency (CTE), since this is relevant only for point sources in low background (Stiavelli 1996), and also given the uncertainties associated with the available algorithm (Holtzman et al. 1995, hereafter H95). In the case of NGC 1700, we forced the isophotes to remain concentric over the whole radial range, and checked *a posteriori* for any bias in the measurements.

Sky subtraction was carried out for some of the galaxies, although the sky level was very small (smaller than 1DN). The sky signal was determined from the WFC images, in areas furthermost from the nucleus. No sky was subtracted from NGC 4406 and NGC 4552, since these galaxies obviously filled the field of view. The uncertainties introduced by not making this correction, or any contamination by the galaxy of the "sky" regions, were estimated to be negligible. This was verified by comparison with ground-based photometry in the overlap region. Good agreement in the radial variation of the surface brightness was found between our outer surface brightness profiles and the ground-based photometry published by Sparks et al. (1991), Goudfrooij et al. (1994a), and Møller et al. (1995).

The photometric zero-point was derived and converted to the Johnson-Cousins system

following the iterative procedure described in H95. For all the galaxies, we first set

$$\begin{aligned} mag_j^o &= -2.5Log(counts/sec) + Z_{WFPC} \\ &\quad +2.5Log(GR) + 5Log(0.046) + 0.1 \end{aligned} \tag{1}$$

with the subscript j indicating either the V or the I filter, Z_{WFPC} the zero point of the filter (equal to 21.724 for F555W, and to 20.840 for F814W; see Table 7 of H95), and GR the gain ratio (set to 1 for gain 15, and to 1.987 for gain 7). The subsequent term accounts for the pixel size. The constant shift of 0.1 mag was added following H95 in order to correct for infinite aperture. Then we iterated the calibration until convergence by inserting the newly derived color term in Eq. (8) of H95, i.e.:

$$mag_j = mag_j^o + c_1(V - I) + c_2(V - I)^2 \tag{2}$$

with $c_1 = -0.052$ and $c_2 = 0.027$ for the V filter, and $c_1 = -0.063$ and $c_2 = 0.025$ for the I filter (Table 7 of H95). The final surface brightness profiles were corrected for Galactic extinction (see Table 1). K-corrections were also applied (Whitford 1971), though they were always smaller than 0.03 mag.

Comparison with the ground-based photometry of Goudfrooij et al. (1994a) and Møller et al. (1995) showed small zeropoint offsets in some cases. These were generally smaller than ~ 0.1 mag. There was no detectable systematic difference in the $V - I$ colors between our HST measurements and the ground-based results ($\Delta(V - I) \lesssim 0.05$ mag).

2.3. Ellipse Fitting Procedure

We modeled each galaxy by means of an iterative procedure which fits isophotes to both V and I final images. The software package used was *galphot* (Jørgensen et al. 1992).

For all the galaxies, fits to derive the isophotal morphological parameters were performed on the V and I frames, after masking out stars and other point-like sources. Most of the galaxies of our sample show extensive dust patches close to their centers. In order to minimize their effects on the determination of the surface brightness profiles in the heavily obscured nuclei, we adopted a modified version of the procedure described by F95. These authors had only one filter (V) available. They determined a maximum radius of influence for the dust (i.e., the "dust radius") and fixed the isophotal properties (ellipticity and position angle) to a constant value inside this radius. The values adopted were chosen equal to the one just beyond the dust radius. The patchy-dust areas were then masked out, and the surface brightness on each isophote (of fixed ellipticity and position angle) inside the dust radius was finally computed.

The availability of two filters allowed us to improve on the above procedure. We used a simple "screen-model" to obtain a rough estimate of the dust absorption from the patchy variations of color over the image (see Appendix A). This model is very simplistic, and is not more than a first order approximation to the complex effects of dust. None the less, visual inspection of the resulting "dust-improved" $I_{improve}$ images showed that the effects of patchy dust were indeed decreased. We used these images to obtain "dust-improved" values for the isophotal parameters, the ellipticity and the position angle. We tested whether these parameters were sensitive to details of the model, such as the location of the screen. We found no significant variations.

The values of ellipticity and position angle obtained from the fits to the dust-improved $I_{improve}$ frames were then kept fixed in a successive iteration of the ellipse fitting to the raw I and V images, in which the heavy dust patches had been previously masked out. The so-obtained surface brightness profiles, which we will refer to as to the *final dust-improved profiles*, were used in the remainder of our analysis. Obviously, this procedure was not

applied to those galaxies devoid of heavy dust patches in their nuclei. For these objects, the straight application of the isophotal fitting package to the raw I and V images (masked for stars and other spurious sources) already provided excellent fits, i.e. the 'final' surface brightness profiles. More details on the procedure adopted for deriving the surface brightness profiles in the heavily obscured nuclei are given in Appendix A.

2.4. Maps of $V - I$ Color

The HST Point-Spread-Function (PSF) depends on position on the CCD. Since no pointlike sources with adequate S/N located near to the nuclei were available for any of the objects, we computed the appropriate V and I PSF for each galaxy by running Tinytim (Krist 1992). This is the optimal procedure in such cases, given the fact that archival stars can not be used due to the presence of focus drifts (occurring on timescales of a few months), breathing (occurring on timescales of a few minutes), and jitter (varying from exposure to exposure). Extensive use has been made of the Tinytim PSFs, and while some concerns may remain, they are second order effects, and the use of a first order correction is certainly better than none at all.

In order to derive the $(V - I)$ color maps and color profiles, the V and I final frames were matched to the same PSF by convolving each band with the PSF of the other band (i.e., $V - I \equiv -2.5log\left(\frac{F^{V}_{conv,obs}}{F^{I}_{conv,obs}}\right)$, where the subscript *conv* stands for convolved images, and F_{obs} are the counts in the image frames). The relative centering of the V and I convolved images was checked before generating the maps; in the case of NGC 1427, we aligned the V image to the I image after rebinning to a quarter of the pixel size. The PSF-matched color profiles were derived by subtraction of the V and I surface brightness profiles obtained by applying the same ellipse fitting procedure described in Section 2.3 to the V and I

PSF-convolved images. Separate measurements of F^V and F^I within apertures of $0.5''$, $1''$, $2''$, and $5''$ of radius were made in order to obtain the $V-I$ color within those apertures.

The current data set does not allow us to derive accurate estimates for dust extinction. However, we used the method of Goudfrooij et al. (1994b) to derive a first order estimate. We computed:

$$A_\lambda = -2.5 log\Big(\frac{F^\lambda_{conv,obs}}{F^\lambda_{conv,mod}}\Big), \tag{3}$$

where $\lambda \equiv I$ or V, and F_{mod} is the number of counts in the isophotal fit models of the PSF-convolved frames. The mean extinctions $A_{V,apert}$ and $A_{I,apert}$ inside an aperture of $5''$ were computed after masking the pixels with $A_V \geq 0.03$ on the A_V and A_I frames. The corresponding values of color excess $E(V-I)_{apert} \equiv A_{V,apert} - A_{I,apert}$ were derived. Typical values are $E(V-I)_{apert} \simeq 0.02$ and $A_{V,apert} \simeq 0.05$, with internal errors smaller than $\approx$ 0.008 and 0.005 magnitudes, respectively.

3. Results

3.1. Isophotal Parameters

The *final, dust-improved* (§2.3) V and I surface brightness and $V-I$ color profiles, and the isophotal morphological parameters derived from the isophotal fits to the (star-masked) V and I images, are given in Figure 1. They will be made available in computer format on request. A comparison with the `WF/PC` F555W profiles of F95 and L95 is presented in Appendix B.

The third and fourth order sine and cosine terms indicate deviations of the isophotes from a pure ellipse as described in terms of a Fourier expansion. In particular, a positive fourth order cosine term indicates a disky structure, while a negative value for this coefficient indicates boxy isophotes (e.g., Lauer 1985).

The color profiles systematically show scatter (< 0.05 mag, peak-to-peak) of a few points in the radial range from about 5" to 9". The inspection of the residual frames does not reveal any obvious cause for this small scatter.

3.2. Individual Properties of the Galaxies

The PSF-matched $V - I$ color maps for the 15 galaxies of our sample are shown in Figure 2 (Plate XX). Each of the panels is $6'' \times 6''$ in size. The frames are rotated so as to align horizontally the major photometric axis of each galaxy. Many galaxies possess a number of features visible at small galactocentric radii. In particular, as already noted by F95, most of the objects show a significant amount of patchy dust inside $1''$. At the distances of our galaxies, the detected features occur on scale lengths of the order of a few tens of parsecs. In the following we describe, separately for each galaxy, the details of the isophotal properties derived from the fits to the V and I frames, and the main features detected in them.

NGC 1427 A visual inspection of the images shows a position angle twist inside $\sim 0.2''$, and very round isophotes inside this radius (as indicated by the decrease in the ellipticity profile inside $\sim 0.3''$). Although dust is not obvious in any of the (residual and original) images, the $V - I$ color map shows two lanes, running parallel to the minor axis and symmetric with respect to the center. Their orientation is perpendicular to a red elongated

structure (inside $\sim 1''$, oriented along the major axis). The color map shows also some evidence for a redder color of the central structure compared to surrounding regions. The fit to the dust improved I frame enhances the isophotal twisting. The C_4 peaks around $1''$, where it reaches the value of ~ 0.01, and decreases from there on, reaching slightly negative values outside $10''$. The other Fourier terms are negligible over the range $0.3'' - 15''$. These features all together indicate the presence of a stellar disk between $0.3'' - 3''$ (which was suspected – although not detected – by F95).

NGC 1439 The nuclear dust lane (at $\sim 0.4''$) detected by F95 is clearly identified with a ring in the color map. SE of the nucleus and adjacent to the ring, a red excess is detected (Figure 3). The ring is centered on the galaxy nucleus, has an apparent inclination of $\sim 50°$ (assuming an intrinsic axial symmetry and $90° \equiv$ edge-on) and an extent of about 40×65pc. The isophotal parameters are affected for radii less than the ring radius. There may also be some effect on the inner color profile. From the ring outward, the morphological parameters are unaffected by the dust, and show a sharp decrease in ellipticity from about $1''$ to $2.5''$. The ellipticity peaks again at $\sim 6''$, where also the C_4 suddenly rises to ~ 0.015, and the isophotes show a small but sudden change of position angle. This provides evidence for the presence of a stellar ring at those radii. Its average color is similar to that of the nearby stellar population.

NGC 1700 Patchy dust and filaments are present in the innermost $2''$, and influence the isophotal shape parameters inside $\sim 0.3''$. The patches are visible in the $V - I$ color map, which also shows a spiral-like structure in the innermost $2''$ (200pc). The galaxy is boxy inside $3''$ ($C_4 \sim -0.01$), and disky outside this radius ($C_4 \sim 0.01$). The ellipticity continuously rises outward, and shows structure clearly identified with the variations in the fourth order cosine term. The disky isophotes and the peak in ellipticity indicate the

presence of a stellar disk between $3''$ and $10''$. No difference in color is seen between this disk and the surrounding galaxy.

NGC 3608 The galaxy appears very round in the nucleus. The ellipticity profile continuously rises with radius, albeit not very smoothly. The C_4 shows a bump around $\sim 0.3''$. S_3 is also rather large at that radius, but is smaller in the fit to the dust-improved I frame. This, and the slight decrease in ellipticity in that radial range, suggests that the observed features are actually due to the presence of some patchy dust. This is apparent from visual inspection of the residual V image, and of the $V-I$ color map, which shows structure inside the innermost $0.6''$ (30 pc). This feature appears elongated along the major axis, and is reminiscent of a (weak) offcentered ring. Outside $5''$, the galaxy is slightly boxy.

NGC 4278 One side of the galaxy is heavily obscured by large-scale dust located NNW of the nucleus. The dust distribution is far from settled, and seems to spiral down into the nucleus. Its distribution shows several dense knots, interconnected by filaments. The filaments are roughly perpendicular to the extended radio emission. The densest and largest of the knots appears about $5.4''$ N of the nucleus, and is ~ 12 pc in size. The large amount of dust dominates the higher-order terms of the Fourier expansion. These are reduced to zero in the fit to the dust-improved I frame, demonstrating the effectiveness of this procedure. The color profiles rise from the very center to $\sim 1''$, and decrease toward bluer values outside this radius. A central point source has been found ($V \simeq 19.7$, $M_V \simeq -9.6$, $V-I \simeq 0.9$). It is bluer than the surrounding stellar population (see the $V-I$ profile). In addition, there is a weak indication from the $V-I$ color map that the stellar population surrounding the central point source is also bluer than the surrounding galactic regions (note the slow increase in Figure 1 in V_I to a radius of $\sim 1''$).

NGC 4365 The nucleus of this galaxy is very diffuse, i.e., the surface brightness profile increases toward the center with a shallow slope. However, it shows a weak (bump-like) excess of brightness in the very center ($V \sim 23$, $M_V \sim -7$) which might be unresolved. Visual inspection of the V image confirms the rounding of the isophotes in the very center ($r \leq 0.3''$) shown by the ellipticity profile in this passband. The I image, instead, shows a weak disk-like feature, which explains the larger ellipticity of the I profile at those radii. A $\sim 40°$ isophote twist is also observed there. In our $V - I$ color map this central tilted structure has a radius of about $0.14''$, and is bluer by about 0.05 mag than the surrounding regions. It seems unlikely that this feature is an artifact of an imperfect matching of the V and I PSFs, since its size is a factor four larger than the FWHM of both Tinytim PSFs. At larger radii, a stellar disk (not seen by van den Bosch et al. 1994, but detected by Forbes 1994) is clearly visible between $1''$ and $3''$. At these radii, the ellipticity and the C_4 show the typical bump, where C_4 reaches 0.01. There is a hint that this disk is slightly redder than the outer surroundings.

NGC 4406 There is a slight decrease in the surface brightness in the region surrounding the very center of NGC 4406 (out to $\sim 0.4''$ radius). The shape of the obscuration is reminiscent of a nuclear dust ring or torus seen close to face-on. This ring appears extended along the minor axis, i.e., its axis is aligned with the stellar kinematic axis of the outer galaxy (which is tilted 90° with respect to that of the core). The ring is hardly seen in the $V - I$ color map, i.e., it does not give rise to a large amount of reddening. However, it induces the large scatter in the isophotal parameters inside $\sim 1''$ (since the scatter is reduced in the fit to the dust-improved I frame). Outside this radius, the isophotal parameters are well defined, and show a transition between an internal stellar disk ($\sim 1'' - 6''$) and outer boxy isophotes. The transition is accompanied by a very weak ($\leq 10°$) isophote twist. No associated structure is seen in the $V - I$ color map (although at those radii the S/N might

be inadequate).

NGC 4494 A very sharp dust ring (well-aligned with the apparent major axis, as was seen also by F95) is visible in the V and I images, and in the $V-I$ color map. The disk is centered with respect to the galaxy center, but its intensity distribution is asymmetric, with the extinction minimum occurring at ~ 10 pc from the center. This is very likely due to projection effects. In fact, its N and NW sides produce a heavier reddening in the $V-I$ color map, and thus are possibly closer to us. Assuming intrinsic circular geometry, the apparent inclination of the ring is 60°, and its projected size roughly 90 pc $\times$ 50 pc. The color map shows an asymmetry in the region surrounding the disk, which, as in NGC 1439, is redder on the far side of the ring. The color profile shows a bump at the position of the ring, and it is possibly influenced also at smaller radii. Outside $\sim 1''$ the isophotal parameters are not affected by the dust ring. From that radius out to about $5''$, the ellipticity drops rapidly from ~ 0.25 to ~ 0.15, and the C_4 from 0.05 to zero. A very small ($\sim 10°$) isophotal twist occurs in the same region. The regularity of the remaining Fourier terms confirms the presence of a stellar disk inside $5''$.

NGC 4552 The nucleus of this galaxy is obscured by an arc-shaped dust lane which runs NE of it. The lane is clearly visible in the V image and in the $V-I$ color map, in which it resembles an incomplete (asymmetric) ring. More extended, radially elongated, filaments are also visible in the frames. Inside about $0.4''$, the isophotal parameters are strongly affected by the dust. Outside $\sim 1''$ the isophotes become very round, a small isophotal twisting is present, and the higher Fourier terms are negligible. The $V-I$ color profile shows a bump inside $\sim 0.25''$, most likely due to the nuclear dust. The central point source, reported as variable in the UV by Renzini et al. (1995), is seen in our frames ($V \simeq 20.6$, $V-I \simeq 1.5$ mag). A detailed analysis of this and of the other two points sources detected

in NGC 4278 and IC 1459 will be reported elsewhere.

NGC 4589 Large scale patchy and filamentary dust perturbs the appearance of the galaxy all across the PC chip. The major dust lane runs almost N-S (i.e., parallel to the minor axis) out to $\sim 10''$, and spatially coincides with the position angle at which Møllenhof & Bender (1989) observed the highest gas rotation velocity (± 200 km s^{-1}; see also F95 and references therein). This lane passes close ($\sim 0.1''$) to the apparent center, which is located in a local minimum of extinction. Around the nucleus and to its west, a more irregular dust distribution is seen, including a cross-like feature ($\sim 9''$ away). The large amount of dust affects the morphological analysis, which shows a drop in ellipticity in the range $0.1'' - 4''$, and relatively large values for the higher coefficients. All these features are much reduced in the fit to the dust-improved I frame.

NGC 5322 A completely obscuring dust lane, which is most probably a nearly edge-on disk perpendicular to the broad radio-jet (Hummel et al. 1984), cuts the nucleus in two, and hides the very center of the galaxy. In the color map, the disk reaches a central value of $V - I = 1.62$, and remains on average about 0.25 mag redder than the surroundings. A red excess is detected in the region adjacent to the disk, S of the galaxy. The isophotal fitting within $\sim 2.5''$ is completely dominated by the strong dust absorption, as is clearly shown from the very large scatter in both the Fourier terms and the position angle. Inspection of the residual maps shows that the sharp decrease in ellipticity towards the center is also an artifact of the fits. Outside $2.5''$, the fits reproduce the morphology of the galaxy quite well. The ellipticity drops significantly, together with C_4 which drops from 0.02 to -0.005, indicating a transition from disky to boxy isophotes. This provides strong evidence for an embedded stellar disk from $\sim 1.5''$ out to $\sim 8''$.

NGC 5813 A dust lane runs parallel to the major axis, East of the nucleus, and contributes to producing the elongated appearance of the central regions. The extremely high values of ellipticity (and the scatter in the Fourier coefficients) are an artifact of the dust lane, and are partially reduced in the fit to the dust-improved I frame. Dust is visible in the $V-I$ color map between the two apparent nuclei, indicating that the double nucleus is an artifact of dust obscuration. Dust filaments are visible within $\sim 7''$, and, quite interestingly, are radially oriented toward the galaxy center. In the $V-I$ color map, two of these filaments are clearly visible (oriented E and S, respectively). They are ~ 0.15 mag redder than the surrounding regions, and reach a $V-I$ value of 1.53 mag.

NGC 5982 The galaxy is extremely round within the innermost $1''$. The scatter of the other isophotal parameters in this region is larger than the measurement errors, and is due to the shallow intensity slope. At $\sim 1''$, a sharp increase in ellipticity and decrease in C_4 is observed. The galaxy remains flattened and boxy ($C_4 \sim -0.02$) from $1''$ outwards. This behaviour might indicate the presence of a face-on stellar disk which dominates the inner region of an otherwise boxy galaxy. A second possibility, also suggested by F95, is that it is an end-on bar that dominates the optical light. Finally, it is also possible that the galaxy is intrinsically round in the nucleus. The color profile is remarkably flat at all radii; the $V-I$ color map shows an elongated feature E of the nucleus, about 0.03 mag redder than the surrounding region.

NGC 7626 A warped, symmetric dust feature (radius $0.45''$, seen also by F95) crosses the very center of the galaxy, and heavily obscures it. It influences the isophotal parameters inside its radius. These show a very steep increase in ellipticity which disappears in the fit to the dust-improved I frame. The lane is tilted by $\sim 35°$ with respect to the radio jet (Jenkins 1982). A $20°$ twisting between $1''$ and $10''$ is observed. This twist is barely

significant, given the low ellipticity of the isophotes. The $V-I$ color map peaks at the very center of the dust lane, with a value of 1.55 mag. The entire dust lane is on average ~ 0.12 mag redder than the surroundings. The color profile shows a continuous, significant decrease with radius.

IC 1459 A heavy dust lane is present in the innermost $\sim 1.1''$, tilted at $\sim 15°$ from the apparent major axis. The lane is asymmetric with respect to the center, although it is present on both sides of it. More chaotic patchy dust is present further away from the nucleus, and other filamentary absorption features show up at $\sim 2''$ from the very center. Inside the dust-lane region, a sharp increase in ellipticity (whose amplitude is larger in V than in I) is observed, together with $\sim 20°$ twisting and a C_4 large and positive in the I band. However, at the same radii the C_4 values show a large scatter in the V band, as do the other terms of the Fourier expansion. All these features are much reduced in amplitude in the isophotal parameters derived from the dust-improved I frame. We conclude that the major features are induced by the dust rather than by real variations in the galactic structure or in the stellar population, and that there is little photometric evidence for the nuclear stellar disk suggested by the analysis of the line-of-sight velocity distribution (Franx & Illingworth 1988). The $V-I$ color map traces the dust distribution, and suggests the presence of a spiral-like structure reminiscent of that detected on larger scales on deep photographs (Malin 1985), and also from the ionized gas distribution (e.g., Forbes et al. 1990). The central point source ($V \simeq 18.4$, $M_V \simeq -12.7$) already detected by F95 stands out in the color map due to its $V-I$ color (~ 1.0 mag), which is bluer than the surrounding stellar population.

3.3. Nuclear Colors and Color Gradients

The nuclear colors derived with radial apertures of $0.5''$, $1''$, $2''$ and $5''$ on the V and I images are reported in Table 2, together with the logarithmic gradients $\frac{d(V-I)}{dLogr}$ between $0.25'' \rightarrow 1.5''$ and $1.5'' \rightarrow 10''$. The logarithmic color gradients should be rather robust against contamination by patchy dust, since the V and I profiles were obtained from isophotal fits to dust-masked frames (Sections 2.3 and 2.4). Both the straight comparison of the different apertures and the inner logarithmic gradients show that radial variations of $V-I$ exist in the innermost $1.5''$. However, the galaxies with the best determined measurements (e.g., those with no contamination of point sources or dust lanes) show inner gradients shallower than the outer gradients (Figure 4). For example, NGC 5982, one of the very few galaxies of our sample without any obvious dust in the field of view of the PC, shows a rather shallow color gradient inside $1.5''$. Furthermore, galaxies with the highest central dust obscuration have the steepest inner color gradients. Another (apparently) dust-free galaxy of our sample, NGC 4365, shows instead a reversal in its color gradient. The positive gradient of NGC 4365 arises from the central blue region (about 15pc in size) detected in its color map.

4. Analytical Description of the Nuclear Properties

4.1. Parametrization of the Surface Brightness Profiles

A few analytical expressions have been proposed to date for describing the surface brightness profile in the inner regions of ellipticals (e.g., F95; L95). Here we chose to use the analytical representation introduced by L95 (and extensively used by Byun et al. 1996), thereby ensuring that a direct comparison could be made between the core properties of "normal" ellipticals and those with kinematically-distinct cores. This expression is:

$$I(r) = 2^{(\beta-\gamma)/\alpha} I_b (\frac{r_b}{r})^{\gamma} \Big[1 + (\frac{r}{r_b})^{\alpha}\Big]^{(\gamma-\beta)/\alpha}. \quad (4)$$

The parameter γ measures the steepness of the rise of the profile toward the very center (i.e., the value of γ in $I(r) \sim r^{-\gamma}$ as $r \rightarrow 0$), r_b is the break radius where the profile flattens to a more shallow slope (in some cases), β is the slope of the outer profile, α controls the sharpness of the transition between inner and outer profile, and I_b is the surface brightness at r_b. For the galaxies where a continuous rise of the surface brightness profile is observed down to the resolution of the data, the L95 law is underdetermined. However, it still yields a very useful, smooth analytical representation of the data. Given the undersampling of the `WFPC2` PSF, we did not perform any PSF-deconvolution, but chose instead to convolve the models with the `WFPC2` PSF before comparing them to the data. The models also included a point source as necessary.

The fitting procedure was carried out in two steps. The first step isolated the true minima of χ^2 from secondary minima. The values of the χ^2 parameter were computed on a number of points regularly distributed on a wide hypercube in parameter space (with dimension equal to the number of free parameters), and once a minimum value was found, a new, smaller, hypercube was placed on that location, and the procedure iterated. The minimum value found on the hypercube was then used as starting point to initialize a downhill simplex minimization. This procedure was tested on simulated data, and found to recover the initial values with high accuracy.

We accepted as final the fits associated with the absolute minimum of χ^2. It is not possible to associate probabilities to these χ^2 values, since they are formally correct but not normalized. There are many reasons for this. First, the data points we fit are not statistically independent. Second, flat fielding errors and the systematic mismatch, when present, between the theoretical law [equation (4)] and the observed surface brightness

profiles, conspire so as to make it not trivial to give a strict statistical interpretation of the χ^2 values (see also Byun et al. 1996). By examining in detail the individual profiles, we found that in all cases for which the formal $\chi^2 \lesssim 1$, the fit is excellent, and matches all the features present in the data. The visual inspection of the fits with $\chi^2 \approx 2$ ascertained that their quality was slightly worse than that of the fits with smaller χ^2. None the less, all our fits can be considered to be a good reproduction the light profiles within the errors. The values of r_b, α, β, γ and $\mu_b \equiv -2.5 Log_{10} I_b$ are listed in Table 3 for the fifteen galaxies of our sample. For each of them, we used these smooth representations of the data for deriving (i) the average logarithmic nuclear slopes corrected for PSF and central point sources effects (Section 4.2); (ii) the deprojected density profiles (Appendix C); and (iii) the radius $r_{0.5}$ at which the slope of the best fit surface brightness profile reached the value of 0.5. The latter parameter is a more robust estimate of the bending radius than the best fit value of r_b, which might be sensitive to (e.g.,dust-induced) variations in the surface brightness profile. The values of $r_{0.5}$ are listed in Table 4. There, the value $r_{0.5} < 0.1''$ has been assigned to all those galaxies whose profiles remained steeper that $r^{-0.5}$ down to our resolution limit ($\sim 0.1''$). In order to compare the nuclear properties of kinematically-distinct cores with those of kinematically-normal galaxies, we also derived the $r_{0.5}$ values for the galaxies of the L95 sample (see Appendix D).

4.2. The Average Nuclear Logarithmic Slopes

In order to provide a global representation of the nuclear galactic properties, we computed average logarithmic slopes within a defined radial range. This was taken to be $0.1'' - 0.5''$, i.e., coincident with the range adopted by L95 for deriving an analogous quantity for their sample of normal galaxies. For both the I and V surface brightness profiles, these logarithmic slopes $\langle\gamma_{data}^{I,V}\rangle$ were initially computed fitting the data points in

two separate ways, i.e., through a least-squares fit and an impartial fit. The impartial fit combined the two least-square fits obtained by exchanging the role of the dependent and independent variables. This algorithm is generally statistically more robust than the simple least-squares fit. The two methods gave, within the errors, identical results for the $\langle\gamma_{data}^{I,V}\rangle$ values.

Since these fits to the data do not account for the presence of central point sources or for the effect of the PSF, we also computed the logarithmic slope $\langle\gamma_{fit}^{I,V}\rangle$ (again within $0.1'' - 0.5''$) of the smooth theoretical curves provided by the V and I best fits of equation (4) to the data. Good agreement was found between $\langle\gamma_{fit}\rangle$ and $\langle\gamma_{data}\rangle$, indicative of the stability of the derived logarithmic slopes. The $\langle\gamma_{fit}^{I,V}\rangle$ values are listed in Table 5. As a reminder, a letter is given to identify those nuclei in which dust is present in the form of a nuclear lane (L), of an extended component (E), filaments (F), or of nuclear patches (P). A question mark indicates galaxies where the detection of dust is uncertain, while an asterisk indicates highly obscured nuclei (whose best fit parameters are reported, but should be used with caution).

Compared to the asymptotic values of γ, the values of $\langle\gamma_{fit}\rangle$ have the big advantage of being independent of any particular parametrization of the surface brightness profile. On the other hand, they are more sensitive than γ to distance effects. The more the surface brightness profile deviates from a pure power-law, the more the $\langle\gamma_{fit}\rangle$ values vary with distance (in galaxies with otherwise identical surface brightness profiles). Thus, we also computed the logarithmic slopes $\langle\gamma_{phys}^{I,V}\rangle$ between $10 - 50$ pc (an interval which corresponds to about $0.1'' - 0.5''$ at the average distance of our sample, i.e., $\sim 20h^{-1}Mpc$).

An inconvenience of both $\langle\gamma_{fit}\rangle$ and $\langle\gamma_{phys}\rangle$ is that homologous galaxies differing only by a scale factor would show very different values for these parameters. However, since $\langle\gamma_{phys}\rangle$ does not depend on the distance, it provides a valuable probe for exploring galactic

properties that would be subject to biases from distance uncertainties. A good correlation is found between the $\langle\gamma_{fit}\rangle$ and $\langle\gamma_{phys}\rangle$ values, which suggests that distance effects are not significant in our sample. This is not altogether surprising since the majority of our galaxies typically lie within 10-20 h^{-1} Mpc, and none lie beyond 40 h^{-1} Mpc. The $\langle\gamma^{I,V}_{phys}\rangle$ values, both for the V and I profiles, are also given in Table 5. In the following, we adopt $\langle\gamma^{I,V}_{phys}\rangle$ to represent the projected nuclear properties of the 15 galaxies. As for the $r_{0.5}$ values, we also derived the $\langle\gamma^{V}_{fit}\rangle$ and $\langle\gamma^{V}_{phys}\rangle$ values for the galaxies of the L95 sample (see Appendix D).

5. Discussion

The discovery of kinematically-distinct cores gave support to the growing consensus that these smooth spheroidal stellar systems might actually hide a past of violent mergers, accretions and interactions with other galaxies. Given this colorful picture, some signatures of such a hectic life might be expected in the very centers of these galaxies.

5.1. Properties of Kinematically-Distinct versus Normal Cores

We have summarized the nuclear properties of our sample in Table 6. The galaxies show a wide range in properties: most, but not all have dust, many, but not all show disks, and the intensity profiles fall in both catagories of "shallow cusps", and "steep cusps". There is no unique, qualifying feature in the present sample. For 11 galaxies the dust absorption is low enough that we can make a confident statement about the presence of the stellar disk at a scale comparable to the one of the kinematically-distinct nucleus (typically about 1″). We find that 7 out of the 11 galaxies show evidence for such a disk. Some additional disks

may have been missed because of projection effects (Rix & White 1990). This suggests that such disks are very common in galaxies with kinematically-distinct cores. It is difficult to state whether this is a special properties of such galaxies, since there is no published data set on "kinematically-normal" galaxies based on WFPC2 data. This makes comparison of the relative disk-fractions in normal and kinematically-peculiar galaxies impossible at this time. However, it appears that not all galaxies have a disk on the scale of the distinct core. NGC 1700, for example, is slightly boxy on the scale of the counter-rotating core.

The nuclear intensity profiles of kinematically-distinct cores show a very large range of logarithmic slopes, from almost flat to very steep. The same was observed by F95 with their smaller sample of such objects. The presence of a break in the luminosity profiles is clearly not directly related to the presence of a distinct component. Furthermore, dynamical arguments (Merritt & Fridman 1995) might exclude the possibility that in some of these systems the observed decoupling is due to projection effects of a triaxial figure (e.g., Statler 1991). This, together with the fact that some of the kinematically-distinct cores do not show minor axis rotation (which rules out the models of Statler 1991), provides evidence that the decoupling is often an intrinsic galactic property.

The comparison of the nuclear properties of kinematically-distinct cores with those of galaxies that are (apparently) kinematically-normal reveals a high degree of similarity between the two classes of objects. In Figure 5 the values of $\langle\gamma^V_{phys}\rangle$ are plotted against the absolute V magnitude M_V for the galaxies of our sample (filled squares) and of L95 sample (open triangles). In Figure 6 the values of the break radius $r_{0.5}$ are plotted against M_V, the symbols having the same meaning as in Figure 5. The figures show that the average logarithmic nuclear slopes and break radii of kinematically-peculiar galaxies cover the same range of values spanned by galaxies with normal core kinematics [although a hint is present for kinematically-distinct core galaxies having, when compared to normal galaxies, (i)

intermediate values of $\langle\gamma^V_{phys}\rangle$, and (ii) smaller values of $r_{0.5}$]. The universal behaviour of nuclear slopes with luminosity was noted also by F95 in their smaller sample.

L95 and K95 have pointed out that the global and nuclear properties are closely connected, with small galaxies hosting the steepest nuclei. This trend is confirmed in Figures 7 and 8, where the values of $\langle\gamma^V_{phys}\rangle$ are plotted against the central Mg_2 values of Davies et al. (1987) and the anisotropy parameter $(v/\sigma_o)^*$ (expressed in logarithmic form, with v the maximum rotation velocity and σ_o the central velocity dispersion of the galaxy; from Bender et al. 1992). The abscissas are now essentially distance-independent, and galaxies leave a clear pattern on these planes. Galaxies with steep cusps tend to be fast rotators with a low Mg_2 absorption and large range of stellar densities, while those with shallow cusps tend to be supported by anisotropy in their velocity field, and to have strong Mg_2 absorption and low stellar densities (see also Figure 9). Galaxies with kinematical peculiarities in their cores again closely follow the locus of normal galaxies.

It is a remarkable result that the nuclear morphology and structure of galaxies with kinematically-distinct cores are so similar to (apparently) kinematically-regular galaxies of the same luminosity class. This result is even more puzzling when one considers the wide dispersion in properties of the individual galaxies. Consider, for example, the cases of (i) NGC 1700, where the isophotes are very boxy close to the galaxy center, and switch to a disky shape in a sharp transition with increasing radius, (ii) NGC 4365, where the inner disk smoothly dissolves into an outer boxy structure, and (iii) NGC 5982, where the very round nucleus is embedded in a highly boxy galactic body. These large changes in the shapes of the isophotes suggest that distinct stellar components are present in the galactic potentials, but that the nature of these components can vary quite considerably. Nonetheless, the overlap of the nuclear properties of the kinematically-peculiar galaxies with those of normal galaxies, and their continuity of properties, suggests that the kinematically-distinct cores

may not owe their existence to any particularly exotic event or process. The growth and evolution of the nuclei appears to be closely related to the formation and evolution of the entire galactic bodies, with the cores possibly being a later development, or, alternatively, the kinematically-distinct cores are a statistically possible outcome of universal processes which formed the entire family of ellipticals, and their nuclei.

5.2. Colors and Color Gradients of the Kinematically-Distinct Cores

The radial color profiles of galaxies with kinematically-distinct cores provide a mean to trace variations in the stellar population related to the possible existence of subcomponents. Ground-based photometric studies have not shown any anomalous color gradients for these galaxies (see e.g., Franx et al. 1989, Peletier et al. 1990). However, these studies, as do all ground-based studies, suffer from a (seeing-) limited angular resolution.

In Figure 10 the $V-I$ color derived within an aperture of $5''$ is plotted against the central Mg_2 value of Davies et al. (1987). The spread in $V-I$ is large in our sample and might be attributable to the large amount of dust detected in the nuclei. Some reduction was found when the color was corrected for the average patchy extinction measured within the same aperture on the A_V and A_I maps (as described in §2.4). The correlation $[V-I = 0.76(\pm0.04)+1.70(\pm0.08)Mg_2]$ between the extinction-corrected color and the Mg_2 line strength (which is unaffected by dust) is good, with a linear correlation coefficient of 0.88. This suggests that the nuclear colors provide a reliable (if not unique) characterization of the properties of the stellar populations.

With the exclusion of NGC 4365, the $V-I$ colors of the nuclear cusps are rather normal. By contrast, the central $\sim$ 15pc region of NGC 4365 contains an elongated structure bluer by ~ 0.05 mag than the surroundings. This blue feature might be due to,

e.g., (i) a hole in an otherwise uniform distribution of dust (a rather high dust mass has been inferred for this galaxy, but we do not observe any obvious patchy dust on the the PC image); or (ii) a pure stellar population effect. Assuming an underlying stellar population of 8 Gyrs and [Fe/H]=0.25 dex, the difference in $V - I$ color between the nucleus and its adjacent region implies either an age difference of 3-4 Gyrs, or a metallicity difference of 0.1-0.2 dex in [Fe/H] (see models by Worthey 1994). The total luminosity of this component is $\sim 2.5 \times 10^6$ $L_\odot$, as derived from the total number of counts detected in the V image within an aperture comparable to the size of the feature. Observations of absorption line strengths at the proper spatial resolution are required to confirm the nature of the blue nucleus of NGC 4365, i.e., to confirm that differences in stellar populations between the very nucleus and the surrounding regions might exist in some kinematically-peculiar elliptical galaxies.

We stress that we have not detected any particular features in the color profiles, which might be attributed to the kinematically-distinct cores. Even in the seven galaxies in which photometric evidence for a stellar disk (or ring) has been found, namely NGC 1427, NGC 1439, NGC 1700, NGC 4365, NGC 4406, NGC 4494 and NGC 5322, there is no evidence for any difference between the color of the disk and that of the surrounding regions. The upper limit in the $V - I$ color difference is about 0.02 mag. This difference should be contrasted to the color gradients at larger radii, or the differences between galaxies, which span a range of 0.15 mag in our sample. It is therefore evident that the stellar populations in the nuclei are surprisingly homogeneous. Alternatively, a very finely tuned conspiracy between age variations and metallicity variations much be present to produce very stable colors. High resolution spectroscopy with HST is needed to confirm this result. The spectroscopic indices will be much less sensitive to dust, and can determine whether a “conspiracy” of changes exist to keep the colors constant.

5.3. Infall of a small galaxy and the role of a super massive black hole

The above results might be taken to rule out the scenario that the kinematically distinct cores formed from a merger of a small galaxy with a big galaxy (Kormendy 1984). In the original scenario, the light at the nucleus was dominated by the small galaxy, and a "core-within-a-core" intensity profile was predicted. The nuclear color was predicted to be blue. None of these predictions have been confirmed, as noted by many authors (e.g., Franx and Illingworth 1988). Instead, these authors argued that the distinct components may have formed in-situ, for example in a star burst. Schweizer (1989) argued that full-fledged mergers might produce such structures. One may therefore ask the question whether the dissipationless merger hypothesis has been finally disproven.

It may be too early to do so. For the galaxies with steep cusps, the victim galaxy will be disrupted under most conditions, and no strong population gradient would be expected anyhow. For galaxies with shallow cusps, the presence of super massive black holes may substantial alter the fate of the small, infalling victim galaxy, as argued earlier by F95. If the black hole has a mass comparable to the mass of the shallow cusp, then the tidal force will remain high throughout the whole shallow cusp. We have performed simple, semi-analytical calculations on the disruption of such a small victim galaxy. These calculations are similar to the ones presented by F95, and show that the light of the victim galaxy is distributed in a very regular way over the host galaxy. If M32 is allowed to spiral into IC 1459 and be disrupted by a super massive black hole, then the light contribution would peak in the center at 10%, and decrease in a very regular way at larger radii. No strong color gradients would be produced in this way.

Clearly, full simulations are needed to confirm the simple calculations and to establish what kinematic signatures remain. It is also clear, however, that it is too early to regard models of dissipational infall as impossible on the basis of the absence of color gradients.

To date, the strongest evidence against these models remains the fact that we see nuclear disks being formed in-situ in recent merger remnants.

5.4. Evidence against Concentrated Diffused Dust

Silva & Wyse (1996) have suggested that a shallow nuclear cusp might be observed if diffuse dust were concentrated in the nucleus, even when the stars are actually distributed in a steep cusp. Silva & Wyse's models predict a very steep $V-I$ color gradient associated to the shallow cusp.

Excluding residual effects of the *patchy* dust on the color profiles, strong $V-I$ gradients are not detected in our shallow-cusp galaxies (see Figure 11, in which the inner $V-I$ gradients are plotted against the nuclear slopes $\langle\gamma^V_{phys}\rangle$). This is not what expected if dust were responsible for the nuclear morphology and color gradients. We conclude that diffuse dust is not the origin for the observed shallow cusps.

5.5. Nuclear and Global Properties: Dichotomy or Continuum?

Global and nuclear properties of elliptical galaxies are closely related (e.g., L95, K95): *(i)* average- and low-luminosity ellipticals rotate rapidly, are nearly isotropic, approximately oblate-spheroidal, disky distorted, and (in the K95 terminology) "coreless" (i.e., have steep cusps), and *(ii)* giant ellipticals, essentially do not rotate, are anisotropic, moderately triaxial, boxy distorted, and have "cuspy cores" (i.e., have shallow cusps). This implies that (small) galaxies with powerlaw cusps have acquired or retained, in their luminous components, more angular momentum than (large) galaxies with shallow cusps. The

distribution of logarithmic nuclear slopes of the mass density profiles is bimodal, i.e. it peaks around the values of -0.8 and -1.9 (Gebhardt et al. 1996). K95 proposed that the dichotomy in the observed properties might actually imply a dichotomy in the formation processes that made elliptical galaxies.

However, if our sample is added to that of the 'normal' L95 galaxies, the trends of the nuclear slope versus the global physical parameters are smooth and continuous, i.e. they do not show any sharp separation between small and large, high- or low- angular momentum galaxies. For example, *(i)* at intermediate luminosities (Figure 5) and metallicities (Figure 7), some galaxies show steep stellar cusps, while others have shallow cusps; *(ii)* although on average anisotropic (pressure supported) galaxies have $\gamma^V_{phys} \lesssim 0.5$ and isotropic (rotation supported) galaxies have steeper nuclear cusps, some degree of overlap is present (see e.g. Figure 12, where we plot the nuclear cusp slope versus the dynamical mass scale $M \equiv r_e \sigma_0^2/G$, and distinguish the isotropic from the anisotropic galaxies).

This leaves room to scenarios in which the observed 'dichotomy' in the nuclear slopes actually arises from a *continuous variation* of some parameter(s) governing the galaxy formation and evolution processes. The observational results described so far suggest that one of such parameters might be the amount of dissipation that occurred in the course of galaxy formation. Very likely, small, steep cusp galaxies have suffered from a large amount of dissipation during their formation. The shallow cusp galaxies might be instead the end products of much less dissipative formation processes (e.g., White 1980; Stiavelli & Matteucci 1991). More data are needed to resolve this issue.

6. Conclusions

In this paper we have presented an analysis of WFPC2 F555W and F814W images for fifteen galaxies with kinematically-distinct cores. The color data were used to correct for the effects dust. We have derived surface brightness and isophotal parameter profiles in the two bands, and color maps and radial profiles in $V-I$. The surface brightness profiles were parametrized by using an average logarithmic slope inside 10-50 pc. This was then used to investigate the nuclear stellar properties of the galaxy cores. A similar parametrization was used for the nuclear stellar morphologies for the kinematically-normal galaxies of L95, so as to compare the results obtained for our sample with a reference sample. We deprojected the surface brightness profiles, and investigated the relationship between projected quantities and physical stellar luminosity densities and cusp slopes.

Our main results are:

- There is no unique photometric parameter that distinguishes the galaxies with kinematically-distinct cores. They show a large range in properties on the scale of the kinematically-distinct cores, like their normal equivalents, namely shallow to steep cusps, and small-scale disks and boxiness. Many of the galaxies show dust, often patchy and chaotic, and sometimes distributed in a ring or disk.

- With some possible exceptions, no obvious evidence is found for homogeneous, diffuse dust *confined* to the galactic nuclei. Thus, the nuclear colors are most likely representative of the stellar population properties.

- In one galaxy, namely NGC 4365, the innermost region (15pc in size, for which the total luminosity is $\sim 2.5 \times 10^6$ L$_\odot$) is bluer by about 0.05 mag than the surrounding regions. If this feature is interpreted as due to a variation in the stellar population, synthetic population models suggest an age younger by $\sim$ 3-4 Gyrs (or an $[Fe/H]$ variation of about -0.2 dex) between the feature itself and the adjacent galactic regions.

- The radial logarithmic slopes of the nuclear stellar profiles are found to cover a large range of values, from almost flat to very steep (the slopes γ range from $\sim$ 0.1 to 0.8). Some galaxies show a clear "break radius", whereas other don't. The nuclear cusp slopes of kinematically-distinct core galaxies occupy the same region of parameter space as that occupied by kinematically-normal galaxies. Independent of the core kinematical properties, slowly-rotating, anisotropic, high metallicity galaxies preferentially have shallow cusps, while fast-rotating, low-metallicity galaxies tend to have steep cusps. Despite the bimodal distribution of the cusp slopes, the trends of the cusp slope with global galactic properties might be smooth and continuous, rather than appearing as a distinct dichotomy, as indicated by e.g., K95.

- Photometric evidence is found for faint stellar disks in seven galaxies, namely NGC 1427, 1439, 1700, 4365, 4406, 4494 and 5322. However, no difference in $V-I$ color (< 0.02 mag) between these disks and the surrounding galactic regions is present. These differences are much smaller than the gradients are larger radii, or the color differences between galaxies (0.15 mag). The nuclear populations are either very homogeneous, or finely-tuned conspiracies between age and metallicity variations exist. High resolution spectroscopy with HST is needed to test for the existence of variations in the metal absorption lines.

These data have added new constraints on aspects of the formation process of elliptical and early-type galaxies. While dust has certainly complicated the interpretation of the data on very small scales, techniques that minimize its effect can be used and allow one to extract reliable quantitative information on structures, surface brightness and luminosity density distributions, as well as on the nature of the stellar population in the cores from colors. Comparison of the nuclear with the global properties suggests that kinematically-distinct cores might be the normal outcome of regular hierarchical merging at early epochs, and not

indicative of any unusual late event in the galaxies evolutionary history.

HST spectroscopy will be extremely valuable to study the nuclear structure of the kinematically distinct components. It remains remarkable how these components stand out in the kinematics, and how difficult they are to find in imaging. HST spectroscopy may be able to resolve many of the unanswered questions of this paper.

CMC thanks C. Norman, M. Stiavelli and T. de Zeeuw for useful discussions; the Institute for Advanced Study, Princeton, and the Space Telescope Science Institute, Baltimore, for hospitality. CMC was supported in the initial phases of this work at the Leiden Observatory by HCM grant ERBCHBICT940967 of the European Community, and is now supported by NASA through a Hubble Fellowship grant HF-1079.01-96a awarded by the Space Telescope Institute, which is operated by the Association of Universities for Research in Astronomy, Inc., for NASA under contract NAS 5-26555. This research was funded in part by the HST grant GO-3551.01.-91A.

Appendix A: Deriving the patchy-dust improved isophotal profiles

The images of most galaxies showed evidence for patchy dust absorption. There can be no mistake that these features were due to dust. They could always be characterized as irregular depressions in an otherwise smooth intensity distribution, and they always corresponded to red patches in the color maps. We set out to obtain a simple correction of such absorption, to produce "dust-improved" images. We note that our procedure only "corrects" for the patchy dust absorption, and not for any extended component. Furthermore, it is not a full correction for the dust absorption: it gives only *improved* images.

The procedure is outlined below. It was applied to all galaxies with evidence for patchy

dust.

1. An initial model fit was made for the I band, which is less affected by dust than the V band. This model fit allowed the position and the shape parameters (ellipticity and position angle) to vary freely throughout the galaxy. This procedure was re-iterated after masking out spurious sources (e.g., foreground stars) on the residual frame obtained with the initial model fit ('re-iterated' I model).

2. A V model was obtained while fixing the center and shape parameters (ellipticity and position angle) of the V isophotes to those of the (re-iterated) I model. The same mask as above was used for the spurious sources. Dust-independent, intrinsic color gradients might still be present, since at each radius the V flux on the isophote is a free parameter of the fitting procedure.

3. The assumption was then made that:

$$\frac{F^V_{obs}}{F^V_{intr}} = D + e^{-\tau}(1 - D) \tag{5}$$

$$\frac{F^I_{obs}}{F^I_{intr}} = D + e^{-\alpha\tau}(1 - D), \tag{6}$$

where the subscripts *obs* and *intr* indicate the observed and intrinsic (i.e., which would be observed in absence of dust) emission, respectively, and F^j indicates the counts in band j, with $j = V, I$. The free constant D ranges between 0 (screen in front of the galaxy) and 1 (screen behind the galaxy, not absorbing any light), and $\alpha = \frac{A_I}{A_V}$ is the ratio between the extinction in I and in V. A value of $\alpha = 0.5$ was assumed, consistent with the Galactic extinction law (see, e.g., Rieke & Lebovsky 1985; Cardelli, Clayton and Mathis 1989). The two-dimensional map of τ is the (unknown) optical depth as a function of position.

In the equations above, the observed V and I images provide the F^V_{obs} and F^I_{obs} maps, respectively, and the V and I models derived from the isophotal fits [steps (1.) and (2.)] are assumed to provide the F^V_{intr} and F^I_{intr} maps.

4. A two-dimensional map for the 'absorption' a was defined as:

$$a \equiv \frac{F^V_{obs}/F^I_{obs}}{F^V_{intr}/F^I_{intr}}.. \tag{7}$$

5. By taking the ratio of the equations in step (3.), the absorption a was connected to the optical depth τ:

$$a = \frac{D + e^{-\tau}(1-D)}{D + e^{-\alpha\tau}(1-D)} \tag{8}$$

The above equation can be turned into an algebraic equation for $t = e^{-0.5\tau}$, namely:

$$t^2 - at - \frac{D(a-1)}{1-D} = 0 \tag{9}$$

This was solved to derive the map of τ.

6. A 'dust-improved' $I_{improve}$ frame was derived by using the computed map of τ in the second equation of step (3.).

$$F^I_{improve} = [D + e^{-\alpha\tau}(1-D)]^{-1} F^I_{obs}. \tag{10}$$

For clarity, we use here the subscript *improve* so as to avoid confusion with the I_{intr} map mentioned before [i.e. with the 're-iterated' I isophotal fit model of step (1.)]. Although they are defined by the same equation, I_{intr} is an input frame when τ is unknown, while $I_{improve}$ is an output frame once τ is determined.

7. The isophote fitting procedure was applied to the dust-improved $I_{improve}$ frames. In the resulting morphological profiles, most of the extreme features such as rapid variations of ellipticity or of the position angle, and very high values for the third and fourth order terms of the Fourier expansion of the intensity (which indicate deviations of the isophotes from perfect ellipses), were absent or much reduced in amplitude.

The smoothness of the dust-improved $I_{improve}$ profiles allowed us to improve the determination of the center of ellipses, ellipticity and position angle in the regions strongly affected by dust.

8. The final isophotal fits were performed, on the I and V images masked out of spurious point-sources and of dust, by keeping the center of the ellipses, the ellipticity and the position angle fixed to those derived from the fit to the $I_{improve}$ image. The dust mask was produced by identifying all those pixels strongly obscured by dust on the residual frames derived from the model fits of steps (1.) and (2.).

9. The sequence outlined in steps (3.) to (8.) was repeated for several values for 'screen-location' parameter D. The value of $D = 0$ already provided smooth I maps, devoid of any obvious patchy dust, i.e. already provided smooth profiles for the center of ellipses, the ellipticity and the position angle needed in step (8.). Values of D different from zero (i.e. screens 'inside' the galaxy) did not significantly affect the resulting isophotal morphological parameters. Thus, in our successive analysis, we decided to adopt the $I_{improve}$ frame obtained by setting $D = 0$.

The azimuthally averaged surface brightness profiles resulting from this procedure are termed *final, dust-improved* in our text. They are a much improved representation of the underlying galaxy starlight. Typical errors on the light profiles, estimated from the residuals of the model fits, are ~ 0.02 mag.

Appendix B: Comparison with WF/PC F555W Profiles

F95 and L95 presented F555W profiles for some of the galaxies of our sample. In particular, IC 1459, NGC 1427, 1439, 4365, 4494, 4589, 5982 and 7626 were investigated by F95, while NGC 1700, 3608 and 5813 are included in L95. In Figure 13 we compare our F555W surface brightness, ellipticity, and position angle profiles within $0.1'' - 2.5''$ to those derived from those authors from the WF/PC data. The agreement is generally good, once NGC 1700 and NGC 4589 are excluded from the comparison. For the former, L95 published a profile oriented differently, by about $90°$, and for the latter no isophotal

parameters were reported by F95 due to the extensive dust. For the surface brightness profiles, the three galaxies of L95 are in very good agreement with our measurements (once an average zero-point shift of about 0.05 mag is removed). Also the surface brightness profiles published by F95 for IC 1459, NGC 4365 and NGC 5982 match our profiles quite well. For the remaining galaxies (namely, NGC 1427, NGC 1439, NGC 4494, NGC 4589 and NGC 7626), a systematic discrepancy is found in the innermost $\sim 0.3''$, where the F95 profiles are brighter than the `WFPC2` ones (by $\Delta\mu \lesssim 0.4$ mag). Possible causes for this effect are: *(i)* an imperfect correction for the `WF/PC` PSF via the Richardson-Lucy method in galaxies with steep central cusps. In this respect, it is remarkable that L95 recovered the light profiles in the inner $0.4''$ with a Fourier algorithm, rather than via the standard deconvolution procedure; *(ii)* the use of different dust masks in the obscured nuclei; and *(iii)* the influence of the residual HST PSF on the `WFPC2` profiles. These factors are all potentially problematic, especially on strongly-cusped nuclei.

Appendix C: The Physical Density Profiles

The observed surface brightness profiles were deprojected by means of an Abel inversion (assuming spherical symmetry) in order to derive the physical luminous density ρ (as a function of radius). There are problems associated with the simple-minded use of such an inversion. When used directly on the data this procedure amplifies the fluctuations and errors present in the data. In addition, since the inner profiles are influenced by the PSF, the deprojection of the data is also affected by resolution effects. These effects are minimized by using the smooth galaxy models obtained by fitting equation (4) to the observed profiles, since the PSF was automatically taken into account in our fitting procedure (with the potential risk here of systematic effects if the model does not match extremely well). Thus, in order to obtain an estimate of the reliability of the derived values,

we deprojected both the data and the smooth theoretical models. These two deprojected profiles were mostly in very good agreement. Both deprojections were finally fitted with equation 4 in order to have a parametric representation of the luminous density. For each galaxy, the asymptotic ($r \rightarrow 0$) slope γ_ρ of the fit to the deprojection of the model surface brightness was adopted as representative of the intrinsic slope of the nuclear cusp.

A quality parameter was defined for the deprojections, ranging from zero (least reliable), to 3 (most reliable). This was obtained by averaging between the two approaches the number of times any of the following properties was satisfied: (1) absence of a central point-like source; (2) steepness of the inner surface brightness profile ($\langle\gamma_{fit}\rangle$) smaller than 0.5; and (3) a difference smaller than 0.1 between *(a)* the asymptotic slope γ_ρ derived from the deprojection of the smooth theoretical surface brightness profile, and *(b)* the equivalent quantity computed from the original data.

The quality parameter is listed in Table 7 together with the V luminous density at $0.1''$ and 10 pc in $L_\odot/pc^3$, the deprojected logarithmic slopes in the range $0.1'' - 0.5''$ and $10 - 50$ pc ($\gamma^{V,I}_{\rho,0.1-0.5''}$ and $\gamma^{V,I}_{\rho,10-50pc}$, respectively), and the asymptotic values of $\gamma^{V,I}_\rho$. In the table, all the given values are those derived from the deprojections of the model surface brightness, while the errors are the absolute difference between these estimates and those derived from direct of the data.

In Figure 14 the average logarithmic slope of the V surface brightness profiles $\langle\gamma^V_{phys}\rangle$ is plotted against the corresponding asymptotic slope γ_ρ (for ours and the L95 sample; see Appendix C). As expected (see e.g., K95), the points lie below the line $\gamma_\rho = \langle\gamma^V_{phys}\rangle + 1$; however, the correlation is good. Thus, the relationships of the galactic properties with $\langle\gamma^V_{phys}\rangle$ can be directly translated into relationships with γ_ρ, although the former was adopted in our discussion because of its direct link to the observed data.

Appendix D: Nuclear Cusp Slopes and Densities for the L95 Sample

L95 derived from their V surface brightness profiles a parameter γ_{L95}, defined as the "average slope over the interval $0.1'' - 0.5''$ calculated from the total change in brightness implied by the fitting law (equ. 4) across the radial interval". These values of γ_{L95} should in principle be directly comparable to our $\langle\gamma^V_{fit}\rangle$ values. However, in order to guarantee an unbiased comparison, we judged it safer to derive the $\langle\gamma^V_{fit}\rangle$ values also for the galaxies of L95, starting from their published profiles. For the three galaxies NGC 1700, 3608 and 5813, both the `WF/PC` data of L95 and our `WFPC2` data were available. The values of $\langle\gamma^V_{fit}\rangle$ derived for these galaxies from the two samples are in very good agreement. The largest difference occurs for NGC 1700, the steepest of the three galaxies, and is equal to 0.08. As expected, the agreement between γ_{L95} and $\langle\gamma_{fit}\rangle$ is always very good (Figure 15).

In addition to $\langle\gamma^V_{fit}\rangle$, also the values of $\langle\gamma^V_{phys}\rangle$ and of the break radius $r_{0.5}$ were derived following the same definition adopted for the galaxies of our sample. In Table 8 these measurements are reported, together with the estimates of the break radii published by L95. Those galaxies that are unresolved are indicated by $r_{0.5} < 0.1''$.

Fits to the surface brightness profiles of the L95 sample were deprojected as in Appendix C, to allow direct comparison with our galaxies. The derived physical densities at $1''$ are compared to those published by L95 in Figure 16. Similarly, Figure 17 shows the asymptotic deprojected slopes obtained with our procedure plotted against the values published by K95 (panel a) and Gebhard et al. (1996; panel b). The values published by K95 and Gebhardt et al. (1996) were obtained by means of a non-parametric deprojection. The independent sets of measurements show a good agreement. This strengthens our confidence in the reliability of the deprojected parameters.

In our comparisons with normal galaxies, we excluded NGC 1700, 3608 and 5813 from

the L95 sample. Furthermore, we considered only the L95 galaxies covering the same range of distance as our own sample ($D \leq 40$Mpc).

Name	Type	D	R_e	M_V	$B\text{-}V_o$	Mg_2	X-ray	A_V
NGC 1427	E5	13.19	2.53	-19.77	0.93	0.258	-	0.0
NGC 1439	E1	15.50	3.13	-19.81	0.93	0.269	-	0.05
NGC 1700	E4	40.55	2.72	-21.71	0.93	-	-	0.09
NGC 3608	E2	10.20	1.76	-19.29	0.98	0.312	39.19	0.0
NGC 4278	E1	7.30	1.17	-19.26	0.96	0.291	-	0.08
NGC 4365	E3	10.35	2.82	-20.42	0.99	0.321	39.48	0.0
NGC 4406	E3	10.35	4.50	-21.09	0.89	0.311	40.75	0.08
NGC 4494	E1	11.20	2.49	-20.46	0.90	0.275	-	0.05
NGC 4552	E0	10.35	1.05	-20.20	0.97	0.324	?	0.11
NGC 4589	E2	18.30	3.71	-20.66	0.94	-	39.88	0.03
NGC 5322	E3	21.05	3.63	-21.42	0.89	0.276	39.93	0.0
NGC 5813	E1	15.93	4.39	-20.56	0.94	0.308	-	0.11
NGC 5982	E3	29.92	2.07	-21.35	0.95	0.296	40.45	0.02
NGC 7626	E1P	37.15	6.85	-21.86	1.00	0.336	40.82	0.12
IC 1459	E3	16.55	3.13	-21.20	0.99	0.321	40.45	0.0

Table 1: Parameters for the 15 galaxies of the sample. Column 1: IC/NGC number; Column 2: Morphological Type (from RC2); Column 3: Distance (h^{-1} Mpc; from Faber et al. 1989, or Bender et al. 1992); Column 4: Effective radius (h^{-1} kpc; from Faber et al. 1989, or Bender et al. 1992); Column 5: Absolute V magnitude (mag + 5 log h; Faber et al. 1989, or Bender et al. 1992); Column 6: Corrected $B-V$ color (magnitudes; from Faber et al. 1989, or Bender et al. 1992); Column 7: Central Mg_2 index (magnitudes; from Davies et al. 1987); Column 8: Log[L_x] (h^{-2} erg s^{-1}; from Roberts et al. 1991); Column 9: Galactic extinction in V (magnitudes; from Faber et al. 1989, after assuming A_V=0.75A_B. The extinction in I was derived assuming A_I=0.51A_V).

Name	$V-I$				$d(V-I)/dlogr$	
	$0.5''$	$1.0''$	$2.0''$	$5.0''$	$0.25''-1.5''$	$1.5''-10''$
N1427	1.26	1.25	1.24	1.22	-0.056 ± 0.002	-0.104 ± 0.035
N1439	1.35	1.32	1.29	1.26	-0.199 ± 0.009	-0.100 ± 0.040
N1700	1.36	1.35	1.33	1.31	-0.073 ± 0.002	-0.087 ± 0.012
N3608	1.30	1.30	1.28	1.27	-0.048 ± 0.001	-0.106 ± 0.029
N4278	1.31	1.32	1.33	1.33	0.049 ± 0.003	-0.079 ± 0.019
N4365	1.32	1.32	1.32	1.31	0.022 ± 0.011	-0.053 ± 0.027
N4406	1.31	1.30	1.30	1.29	-0.022 ± 0.002	-0.064 ± 0.005
N4494	1.36	1.31	1.27	1.23	-0.237 ± 0.005	-0.075 ± 0.019
N4552	1.37	1.36	1.35	1.33	-0.046 ± 0.001	-0.072 ± 0.004
N4589	1.46	1.44	1.42	1.35	-0.114 ± 0.002	-0.211 ± 0.014
N5322	1.39	1.33	1.29	1.25	-0.160 ± 0.001	-0.048 ± 0.011
N5813	1.41	1.39	1.38	1.36	-0.056 ± 0.003	-0.116 ± 0.025
N5982	1.27	1.27	1.26	1.26	-0.025 ± 0.003	-0.083 ± 0.042
N7626	1.43	1.41	1.40	1.37	-0.072 ± 0.002	-0.100 ± 0.020
I1459	1.43	1.37	1.36	1.33	-0.104 ± 0.001	-0.084 ± 0.007

Table 2: $V-I$ colors in magnitudes, and logarithmic color gradients for the 15 galaxies. Column 1: Galaxy name. Column 2: $V-I$ color in the $0.5''$ aperture. Column 3: $V-I$ color in the $1.0''$ aperture. Column 4: $V-I$ color in the $2.0''$ aperture. Column 5: $V-I$ color in the $5.0''$ aperture. Column 6: $V-I$ color gradients in the range $0.25''-1.5''$. Column 7: $V-I$ color gradients in the range $1.5''-10''$. For IC 1459, NGC 4278 and NGC 4552, the point sources were subtracted before performing the measurements. Internal errors for the aperture measurements are smaller than 0.01 magnitudes; for the gradients, the formal errors of the fits are reported.

Name	Filter	r_b	α	β	γ	μ_b	χ^2
N1427	V	0.897	1.817	1.339	0.680	16.501	0.55
N1427	I	0.815	1.760	1.349	0.674	15.157	0.44
N1439	V	0.495	23.61	1.326	0.777	16.027	1.65
N1439	I	0.424	20.03	1.338	0.776	14.570	1.95
N1700*	V	0.181	0.462	1.649	0.007	14.582	0.14
N1700*	I	0.179	0.475	1.676	0.007	13.273	0.23
N3608	V	0.453	0.725	1.582	0.003	15.782	1.08
N3608	I	0.418	0.780	1.566	0.003	14.424	0.87
N4278	V	0.894	1.452	1.316	0.	15.982	0.89
N4278	I	1.112	1.252	1.464	0.	14.850	2.30
N4365	V	1.979	1.669	1.460	0.108	16.949	0.85
N4365	I	1.826	1.516	1.489	0.045	15.582	0.59
N4406	V	0.945	4.132	1.046	0.041	16.082	0.20
N4406	I	0.912	3.322	1.075	0.	14.809	0.21
N4494	V	0.840	4.125	1.232	0.613	15.802	1.78
N4494	I	0.700	3.250	1.246	0.604	14.394	1.73
N4552*	V	0.478	2.174	1.056	0.	15.160	0.37
N4552*	I	0.497	2.095	1.083	0.043	13.886	0.39
N4589	V	0.757	0.433	1.622	0.	16.608	1.51
N4589	I	0.541	0.501	1.578	0.009	14.911	0.74
N5322	V	0.705	1.235	1.401	0.	15.875	0.39
N5322	I	0.683	1.107	1.452	0.	14.586	1.10
N5813	V	0.889	1.767	1.414	0.029	16.560	0.69
N5813	I	0.872	1.667	1.456	0.008	15.232	0.53
N5982*	V	0.476	2.155	1.188	0.118	15.890	0.17
N5982*	I	0.472	2.165	1.192	0.117	14.655	0.22
N7626	V	0.406	1.530	1.225	0.001	16.250	1.13
N7626	I	0.390	1.295	1.274	0.	14.910	1.30
I1459	V	1.433	0.959	1.757	0.016	16.248	2.42
I1459	I	1.822	0.807	2.036	0.020	15.148	1.21

Table 3: Structural parameters from the fits of equation (4) to the V and I surface brightness profiles of our galaxies. For some of the galaxies (indicated by an asterisk), the fits had to be restricted within $3''$, in order to better reproduce the nuclear profiles. For the remaining galaxies, the fits were extended to $10''$.

Name	$r^V_{0.5}$	$r^I_{0.5}$
N1427	< 0.1	< 0.1
N1439	< 0.1	< 0.1
N1700	< 0.1	< 0.1
N3608	0.15 ± 0.07	0.16 ± 0.08
N4278	0.64 ± 0.10	0.66 ± 0.10
N4365	1.16 ± 0.08	1.09 ± 0.03
N4406	0.91 ± 0.10	0.87 ± 0.10
N4494	< 0.1	< 0.1
N4552	0.46 ± 0.02	0.44 ± 0.01
N4589	0.12 ± 0.04	0.11 ± 0.32
N5322	0.44 ± 0.19	0.38 ± 0.13
N5813	0.61 ± 0.10	0.59 ± 0.10
N5982	0.36 ± 0.18	0.36 ± 0.18
N7626	0.32 ± 0.20	0.28 ± 0.05
I1459	0.53 ± 0.10	0.43 ± 0.10

Table 4: Values of the break radius $r_{0.5}$ in arcseconds derived from the best fits to the V and I surface brightness profiles as the points at which the (model) nuclear profiles become shallower than $r^{-0.5}$. Galaxies in which this condition was never reached are considered unresolved ($r_{0.5} \leq 0.1''$). Errors are the differences between the $r_{0.5}$ derived from the best model fits, and those obtained directly from the data. In order to obtain the latter values, the point source contribution was subtracted when present, and the data smoothed when too noisy.

Name	Dust	γ^V_{fit}	γ^I_{fit}	γ^V_{phys}	γ^I_{phys}
N1427	$L, ?$	0.74 ± 0.02	0.75 ± 0.02	0.80 ± 0.04	0.82 ± 0.03
N1439	L	0.79 ± 0.03	0.83 ± 0.03	0.86 ± 0.10	0.93 ± 0.10
N1700	P	0.86 ± 0.02	0.87 ± 0.01	0.68 ± 0.08	0.65 ± 0.09
N3608	P	0.59 ± 0.04	0.59 ± 0.04	0.80 ± 0.02	0.82 ± 0.03
N4278	$E, F, *$	0.20 ± 0.05	0.21 ± 0.07	0.53 ± 0.04	0.51 ± 0.04
N4365		0.15 ± 0.02	0.12 ± 0.02	0.24 ± 0.05	0.23 ± 0.04
N4406	$L, ?$	0.05 ± 0.04	0.03 ± 0.02	0.16 ± 0.02	0.18 ± 0.04
N4494	L	0.61 ± 0.04	0.63 ± 0.01	0.67 ± 0.04	0.71 ± 0.01
N4552	L, F	0.23 ± 0.06	0.25 ± 0.06	0.53 ± 0.04	0.54 ± 0.04
N4589	$E, F, *$	0.59 ± 0.01	0.61 ± 0.01	0.60 ± 0.03	0.62 ± 0.01
N5322	$L, *$	0.30 ± 0.02	0.34 ± 0.01	0.29 ± 0.05	0.33 ± 0.04
N5813	F, P	0.17 ± 0.01	0.18 ± 0.02	0.24 ± 0.03	0.24 ± 0.02
N5982		0.34 ± 0.01	0.34 ± 0.01	0.21 ± 0.02	0.21 ± 0.03
N7626	$L, *$	0.38 ± 0.03	0.43 ± 0.01	0.18 ± 0.03	0.22 ± 0.01
I1459	$L, *$	0.34 ± 0.04	0.36 ± 0.05	0.36 ± 0.05	0.41 ± 0.06

Table 5: I and V logarithmic slopes within $0.1'' - 0.5''$ (γ_{fit}) and 10-50pc (γ_{phys}) for the galaxies of the sample. Column 1: IC/NGC number; Column 2: Dust morphology: a nuclear lane (L), an extended component (E), filaments (F), or nuclear patches (P). A question mark indicates galaxies where the detection of dust is uncertain. An asterisk indicates an heavily obscured nucleus. Column 3: Logarithmic slopes of the V surface brightness profiles within $0.1'' - 0.5''$; Column 4: Logarithmic slopes of the I surface brightness profiles within $0.1'' - 0.5''$; Column 5: Logarithmic slopes of the V surface brightness profiles within 10-50pc; Column 6: Logarithmic slopes of the I surface brightness profiles within 10-50pc. Tabulated values are the logarithmic slopes of the best model fits to the data; errors are the differences between these estimates, and those obtained through a straight fit to the data.

Name	Comments	Stellar Disk?	Cusp
N1427	dust inside $r \simeq 0.1''$; disky inside $1''$, boxy outside	Y	steep
N1439	dust ring at $r \simeq 0.4''$; ϵ peak at $1''$	Y	steep
N1700	patchy dust; boxy inside $r \simeq 1$", disky outside	Y	steep
N3608	no significant structure	N	shallow
N4278	extensive dust; blue point source	N	shallow*
N4365	ϵ peak inside $1-5''$; disky inside $\simeq 2''$, boxy outside; blue nucleus	Y	shallow
N4406	dust ring; disky inside $1-5''$, boxy outside	Y	shallow
N4494	strong dust ring; ϵ high near $1''$; slightly disky	Y	steep
N4552	patchy dust inside $r \simeq 0.4''$; filamentary dust outside; point source	N	shallow
N4589	extensive dust	?	shallow cusp*
N5322	strong dust disk; ϵ peak inside 2.5-5$''$; disky	Y	shallow*
N5813	patchy/filamentary dust; no other structure	N	shallow
N5982	strong isophotal twist and low ϵ inside $r \simeq 1''$	Bar?	shallow
N7626	small dust warp; no other structure	N	shallow
I1459	dust lane; somewhat disky outside $r \simeq 1''$; blue point source	?	shallow

Table 6: Nuclear properties of the 15 galaxies of our sample. Column 2: summary of dust and isophotal morphology; Column 3: Y and N indicate the presence or absence of a stellar disk, respectively; Column 4: shape of the intensity profile at the scale of the distinct nucleus. Question marks indicate uncertain detections; asterisks in Column 4 indicate uncertain measurements due to strong dust obscuration.

Name	Filter	$\gamma_{\rho,0.1-0.5''}$	$\gamma_{\rho,10-50pc}$	$\rho^V_{0.1''}$	ρ^V_{10pc}	γ_ρ	Quality
N1427	V	1.63 ± 0.001	1.64 ± 0.06	1765 ± 20	890 ± 20	1.38 ± 0.22	1.5
N1427	I	1.62 ± 0.04	1.65 ± 0.02			1.32 ± 0.10	
N1439	V	1.63 ± 0.06	1.57 ± 0.03	1620 ± 120	1035 ± 50	0.98 ± 0.29	1.5
N1439	I	1.58 ± 0.07	1.60 ± 0.12			1.35 ± 0.09	
N1700	V	1.74 ± 0.10	1.58 ± 0.33	1000 ± 140	2800 ± 1200	1.08 ± 0.19	1.5
N1700	I	1.76 ± 0.13	1.59 ± 0.48			0.82 ± 0.06	
N3608	V	1.34 ± 0.21	1.58 ± 0.33	1380 ± 360	635 ± 55	0.73 ± 0.17	1
N3608	I	1.33 ± 0.22	1.59 ± 0.48			0.84 ± 0.46	
N4278	V	0.47 ± 0.34	1.03 ± 0.04	410 ± 400	295 ± 40	0.17 ± 0.55	1
N4278	I	0.54 ± 0.07	1.03 ± 0.09			0.24 ± 0.23	
N4365	V	0.69 ± 0.33	0.67 ± 0.08	175 ± 55	105 ± 5	0.55 ± 0.01	2.5
N4365	I	0.47 ± 0.25	0.57 ± 0.01			0.35 ± 0.18	
N4406	V	0.26 ± 0.54	0.14 ± 0.45	115 ± 45	85 ± 35	0.18 ± 0.18	2.5
N4406	I	0.00 ± 0.40	0.13 ± 0.44			0.01 ± 0.01	
N4494	V	1.52 ± 0.01	1.44 ± 0.12	2650 ± 200	1060 ± 30	1.48 ± 0.16	1
N4494	I	1.48 ± 0.12	1.48 ± 0.11			1.42 ± 0.24	
N4552	V	0.41 ± 0.14	0.96 ± 0.02	480 ± 80	448 ± 96	0.02 ± 0.43	1.5
N4552	I	0.54 ± 0.17	1.01 ± 0.04			0.26 ± 0.06	
N4589	V	1.43 ± 0.13	1.45 ± 0.09	600 ± 30	535 ± 95	1.04 ± 1.00	1
N4589	I	1.44 ± 0.23	1.46 ± 0.18			0.92 ± 0.92	
N5322*	V	0.73	0.71	260 ± 130	265 ± 90	0.25	2.5
N5322*	I	0.85	0.83			0.03 ± 0.02	
N5813	V	0.42 ± 0.07	0.49 ± 0.02	110 ± 20	105 ± 10	0.44 ± 0.28	2.5
N5813	I	0.40 ± 0.10	0.49 ± 0.05			0.13 ± 0.03	
N5982	V	0.74 ± 0.12	0.63 ± 0.23	1720 ± 30	225 ± 70	0.56 ± 0.38	2
N5982	I	0.74 ± 0.13	0.62 ± 0.23			0.56 ± 0.51	
N7626	V	0.83 ± 0.17	0.47	100 ± 35	115 ± 115	0.15	2
N7626	I	0.98 ± 0.17	0.64			0.58	
I1459	V	0.79 ± 0.40	0.85 ± 0.05	415 ± 555	370 ± 260	0.72 ± 0.05	2
I1459	I	0.93 ± 0.03	0.99 ± 0.13			0.96 ± 0.08	

Table 7: Deprojected average logarithmic and asymptotic slopes, and luminous densities (in L/pc^3), for the galaxies of our sample. Column 1: Name and filter; Column 2: Logarithmic slopes within $0.1'' - 0.5''$; Column 3: Logarithmic slopes within $10 - 50$pc; Column 4: Luminous V densities at $0.1''$; Column 5: Luminous V densities at 10pc; Column 6: Asymptotic slope derived from fitting the analytical law (Eq. 4) to the deprojections of the surface brightness profiles; Column 7: Quality parameter. Errors are the difference between the estimates obtained from deprojecting the model surface brightness profiles, and those obtained from deprojecting the data. Errors are not reported for those cases where the straight deprojection of the data could not be performed. (*) The measurements for NGC 5332 are uncertain, due to the heavy dust obscuration of its nucleus.

Name	$\langle\gamma^V_{phys}\rangle$	$r^V_{0.5,our}$	$r^V_{b,L95}$
N524	0.52 ± 0.04	0.30 ± 0.03	0.33
N596	0.82 ± 0.04	<0.1	<0.08
N720	0.07 ± 0.01	2.44 ± 0.09	3.21
N1023	0.74 ± 0.01	<0.1	<0.05
N1172	1.00 ± 0.06	<0.1	<0.05
N1331	0.59 ± 0.18	<0.1	<0.05
N1399	0.13 ± 0.01	1.73 ± 0.22	3.14
N1400	0.62 ± 0.01	0.18 ± 0.01	0.33
N1426	0.84 ± 0.03	<0.1	<0.05
N2636	0.95 ± 0.07	<0.1	<0.1
N2841	0.76 ± 0.01	0.15 ± 0.09	<0.1
N3115	0.85 ± 0.05	<0.1	<0.05
N3377	1.15 ± 0.04	<0.1	<0.08
N3599	0.95 ± 0.06	<0.1	<0.05
N3605	0.69 ± 0.01	<0.1	<0.08
N4239	0.41 ± 0.01	0.31 ± 0.59	<0.05
N4387	0.72 ± 0.01	<0.1	<0.08
N4434	0.86 ± 0.03	<0.1	<0.05
N4458	1.40 ± 0.08	<0.1	<0.1
N4464	0.97 ± 0.05	<0.1	<0.05
N4467	0.95 ± 0.05	<0.1	<0.05
N4486B	1.16 ± 0.04	0.11 ± 0.03	0.18
N4551	0.81 ± 0.02	<0.1	<0.05
N4636	0.19 ± 0.02	2.04 ± 0.41	3.21
N4697	0.67 ± 0.01	<0.1	<0.05
N4742	1.02 ± 0.01	<0.1	<0.05
N5845	0.51 ± 0.06	0.20 ± 0.15	<0.05
N7332	1.00 ± 0.03	<0.1	<0.05
V1199	1.22 ± 0.21	<0.1	<0.05
V1440	0.99 ± 0.13	<0.1	<0.05
V1545	0.62 ± 0.04	<0.1	<0.05
V1627	1.09 ± 0.17	<0.1	<0.05

Table 8: Values of the average logarithmic slope within 10-50pc ($\langle\gamma^V_{phys}\rangle$), and of the break radius in arcseconds, for the galaxies of the L95 sample within 40 h^{-1} Mpc. Column 2: Tabulated values of $\langle\gamma^V_{phys}\rangle$ are the logarithmic slopes of the best model fits to the data; errors are the differences between these estimates, and those obtained through a straight fit to the data. Column 3: our measurements of $r_{0.5}$, derived from the best fits to the V surface brightness profiles as the points at which the nuclear profiles become shallower than $r^{-0.5}$. In our measurements, we consider unresolved those nuclei in which $r_{0.5} < 0.1''$. Errors are the differences between the $r_{0.5}$ derived from the best model fits, and those obtained directly from the data. Column 4: the measurements of r_b published by L95.

REFERENCES

Bender, R., Burstein, D., Faber, S.M., 1992, ApJ, 399, 462

Byun, Y.-I., Grillmair, C.J., Faber, S.M., Ajhar, E.A., Dressler, A., Kormendy, J., Lauer, T.R., Richstone, D., Tremaine, S., 1996, AJ, 111, 1889

Cardelli, J.A., Clayton, G.C., Mathis, J.S., 1989, ApJ, 345, 245

Crane, P., Stiavelli, M., King, I.R., Deharveng, J.M., Albrecht, R., Barbieri, C., Blades, J.C., Boksenberg, A., Disney, M.J., Jakobsen, P., Kamperman, T.M., Macchetto, F., Mackay, C.D., Paresce, F., Weigelt, G., Baxter, D., Greenfield, P., Jedrzejewski, R., Nota., A., Sparks, W.B.: 1993, AJ, 106, 1371

Davies, R.L., Burstein, D., Dressler, A., Faber, S.M., Lynden–Bell, D., Terlevich, R.J. and Wegner, G., 1987, ApJSS, 64, 581

Faber, S.M., Wegner, G., Burstein, D., Davies, R.L., Dressler, A., Lynden–Bell, D., Terlevich, R.J., 1989, ApJ, 69, 763

Forbes, D.A., 1994, AJ, 107, 2017

Forbes, D.A., Sparks, W.B., Macchetto, F.D., 1990, "Paired and Interacting Galaxies", ed. J. Sulentic, W. Keel, C. Telesco, NASA pub., p. 431

Forbes, D.A., Franx, M., Illingworth, G.D., 1995, AJ, 109, 1988 (F95)

Forbes, D.A., Franx, M., Illingworth, G.D., Carollo, C.M., 1996, ApJ, 467, 126

Franx, M., Illingworth, G.D.: 1988, ApJL, 327, L55

Gebhardt, K., et al., 1996, AJ, 112, 105

Goudfrooj, P., Hansen, L., Jørgensen, H.E., Noorgaard Nielson, H.U., 1994a, AAS, 104, 179

Goudfrooj, P., de Jong, T., Hansen, L., Noorgaard Nielson, H.U., 1994b, MNRAS, 271, 833

Hummel, E., van der Hulst, J.M., Dickey, J.M., 1984, AA 134, 207

Jaffe, W., Ford, H.C., O'Connel, R.W., van den Bosch, F.C., Ferrarese, L., 1994, AJ, 108, 1567

Jenkins, C.R., 1982, MNRAS, 200, 705

Jørgensen, I., Franx, M., Kjærgaard, P., 1992, AAS, 95, 489

Holtzman, J.A., Burrows, C.J., Casertano, S., Hester, J.J., Trauger, J.T., Watson, A.M., Worthey, G., 1995, PASP, 107, 1065

Kormendy, J., 1984, ApJ, 287, 577

Kormendy, J., Byun, Y.-I., Ajhar, E.A., Lauer, T.R., Dressler, A., Faber, S.M., Grillmair, C., Gebhardt, K., Richstone, D., Tremaine, S., IAU Symposium 171, "New Light on Galaxy Evolution", ed. R.L. Davies & R. Bender, Kluwer: Dordrecht, in press (K95)

Krist, J., 1992, Tinytim v2.1 User's Manual (STScI)

Lauer, T.R., 1985, ApJ, 292, 104

Lauer, T.R., Ajhar, E., Byun, Y.-I., Dressler, A., Faber, S.M., Grillmair, C., Kormendy, J., Richstone, D., Tremaine, S., 1995, AJ, 110, 2622

Malin, D.F., 1985, "New Aspects of Galaxy Photometry", ed. J.-L. Nieto, Berlin: Springer-Verlag, p. 27

Merritt, D., Fridman, T., 1996, ApJ, 460, 136

Möllenhoff, C., Bender, R., 1989, AA, 214, 61

Møller, P., Stiavelli, M., Zeilinger, W.W., 1995, MNRAS, 276, 979

Peletier, R.F., Davies, R.L., Illingworth, G.D., Davis, L.E., Cawson, M.C.M., 1990, AJ, 100, 1091

Renzini, A., Greggio, L., di Serego Alighieri, S., Cappellari, M., Burstein, D., Bertola, F., Nature, 378, 39

Rieke, G.H., Lebovsky, M.J., 1985, ApJ, 288, 618

Rix, H-W., White, S.D.M., 1990, ApJ, 362, 52

Roberts, M.S., Hogg, D.E., Bregman, J.N., Forman, W.R., Jones, C., 1991, ApJSS. 75, 751

Schweizer, F., Seitzer, P., Faber, S.M., Burstein, D., Dalle Ore, C.M., Gonzalez, J.J., 1990, ApJL, 364, L33

Silva, D.R., Wyse, M.W., 1996, ApJL, 457, L15

Sparks, W.B., Wall, J.V., Jorden, P.R., Thorne, D.J., van Breda, I., 1991, APJS, 76, 471

Statler, T.S., 1991, ApJ, 382, L11

Stiavelli, M., 1996, private communication

Stiavelli, M., Matteucci, F., 1991, ApJL, 377, L79

van den Bosch, F.C., Ferrarese, L., Jaffe, W., Ford, H.C., O'Connel, R.W., 1994, AJ, 108, 1579

van Dokkum, P.G., Franx, M., 1995, AJ, 110, 2027

White, S.D.M., 1980, MNRAS, 191, 1

Whitford, B.C., 1971, ApJ, 169, 215

Worthey, G., 1994, ApJS, 95, 107

Figure 1. Surface brightness and isophotal parameters as a function of log(radius), in arcsec. Stars are used for the V band, open squares for the I band. From top to bottom, the left panels show the surface brightness μ, the $V-I$ color, the position angle (PA) and the ellipticity (ϵ) profiles; the right panels the third order sine (S_3) and cosine (C_3), and fourth order sine (S_4) and cosine (C_4) terms. In the $V-I$ color panels, dots indicate the original unconvolved profiles; crosses indicate the color profiles obtained after convolution to ensure that the V and I data have the same PSF (see §2.4). The thick solid line indicates the fit to the dust-corrected $I_{improve}$ frames. Formal errors from the ellipse fitting are given for the isophotal parameters. For the surface brightness profiles, errors include sky subtraction. Errors on the $V-I$ values are the quadratic mean of the errors on the V and I bands. The errors are given every three points; when they are not visible, they are smaller than the size of the symbols.

Figure 2. $V-I$ color maps for the 15 galaxies. Each panel is $6'' \times 6''$. The photometric major axes are aligned with the abscissa. Redder regions are darker. From left to right, first row: NGC 1427, NGC 1439, NGC 1700, NGC 3608; second row: NGC 4278, NGC 4365, NGC 4406, NGC 4494; third row: NGC 4552, NGC 4589, NGC 5322, NGC 5813; last row: NGC 5982, NGC 7626, IC 1459.

Figure 3. Three cuts across the $V-I$ color map of NGC 1439. Each cut is the average within a strip 7 pixels wide, running parallel to the major axis. The solid line passes through the galaxy center; the dotted line is to the N, and the dashed to the S. The sharp dust ring is symmetric with respect to the galaxy center. An area of weaker reddening surrounds the ring. This area is more extended on the far side of the ring.

Figure 4. Comparison of inner ($0.25'' - 1.5''$) and outer ($1.5'' - 10''$) $V-I$ color gradients for the galaxies of our sample. The galaxies with the best determined

measurements are plotted as filled squares.

Figure 5. Projected nuclear logarithmic slope $\langle\gamma^V_{phys}\rangle$ versus absolute magnitude M_V. Filled squares are our kinematically-distinct core galaxies, open triangles the "normal" L95 galaxies.

Figure 6. Logarithm of break radius $r_{0.5}$ (in pc) versus absolute magnitude M_V. Filled squares are our sample, open triangles the L95 galaxies. Galaxies with values of $r_{0.5} < 0.1''$ are not included in the plot. The solid line shows the value of $r_{0.5}$ in pc corresponding to $0.1''$ at the closest distance of our sample (7.3 h^{-1} Mpc). The arrow indicates the effect of an error of 50 % in the distance.

Figure 7. Projected nuclear logarithmic slope $\langle\gamma^V_{phys}\rangle$ versus central Mg_2 values (in magnitudes; from Davies et al. 1987). Filled squares are our sample, open triangles the L95 galaxies.

Figure 8. Projected nuclear logarithmic slope $\langle\gamma^V_{phys}\rangle$ versus values of the anisotropy parameters $(v/\sigma_\circ)^*$ (from Bender et al. 1992). Filled squares are our sample, open triangles the L95 galaxies.

Figure 9. Values of stellar densities at 10pc, in $L_\odot/pc^3$, versus central Mg_2 (in magnitudes; from Davies et al. 1987). Squares are our sample, triangles the L95 galaxies. Open symbols are for galaxies with $\langle\gamma^V_{phys}\rangle < 0.5$, filled symbols for galaxies with steeper slopes.

Figure 10. Measurements of $V - I$ inside $5''$ versus the Mg_2 values of Davies et al. (1987; filled triangles). Units are magnitudes along both axes. Internal errors on the aperture measurements of $V - I$ are negligible. The 6-point stars are obtained by correcting

the $V - I$ measurements for reddening (using the values of $E(V - I)_{aperture}$, see §2.4). The good correlation supports that the nuclear $V - I$ is not strongly affected by dust, and is thus a reliable indicator of the properties of the stellar populations in the central cusps.

Figure 11. Logarithmic $V - I$ color gradients inside $0.25''$-$1.5''$ versus $\langle\gamma^V_{phys}\rangle$. Identified are the galaxies with heavy patchy dust, or dust lanes.

Figure 12. Dynamical mass scale $logM = log(\sigma_o^2 r_e/G)$, in $M_\odot$, versus the nuclear logarithmic cusp slope $\langle\gamma^V_{phys}\rangle$. The squares are our sample of kinematically-distinct core galaxies, and the triangles are the galaxies of L95. Filled symbols are anisotropic galaxies with $log(v/\sigma_o)^* < -0.3$, open symbols are isotropic rotators, where $log(v/\sigma_o)^* > -0.3$. The values of σ_o, r_e and $log(v/\sigma_o)^*$ are from Bender et al. (1992).

Figure 13. Comparison with the `WF/PC` F555W data of F95 and L95. Each panel contains, from top to bottom, the position angle PA, the ellipticity ϵ, and the V surface brightness profiles. First row, from left to right: NGC 1427, NGC 1439, NGC 1700, NGC 3608; second row, left to right: NGC 4365, NGC 4494, NGC 4589, NGC 5813; third row, left to right: NGC 5982, NGC 7626, IC 1459.

Figure 14. Luminosity density, V band, deprojected asymptotic logarithmic slopes γ_ρ versus projected average nuclear slope $\langle\gamma^V_{phys}\rangle$. The $\gamma_\rho = \langle\gamma^V_{phys}\rangle + 1$ line is plotted for reference.

Figure 15. Comparison between the logarithmic slopes γ_{L95} and $\langle\gamma_{fit}\rangle$ for the L95 sample (see text).

Figure 16. Luminous density at $0.1''$ (in $L_\odot/pc^3$) derived by L95 and from this work.

Figure 17. Panel (a): Deprojected asymptotic logarithmic slopes derived by Kormendy et al. (1995) and from this work for the six galaxies of the L95 sample with shallowest nuclear slope. The filled symbol represents NGC 6166, for which the errorbars are very large along both axes. Panel (b): Deprojected asymptotic logarithmic slopes derived by Gebhardt et al. (1996) and from this work for those galaxies for which both methods provided reliable slopes.

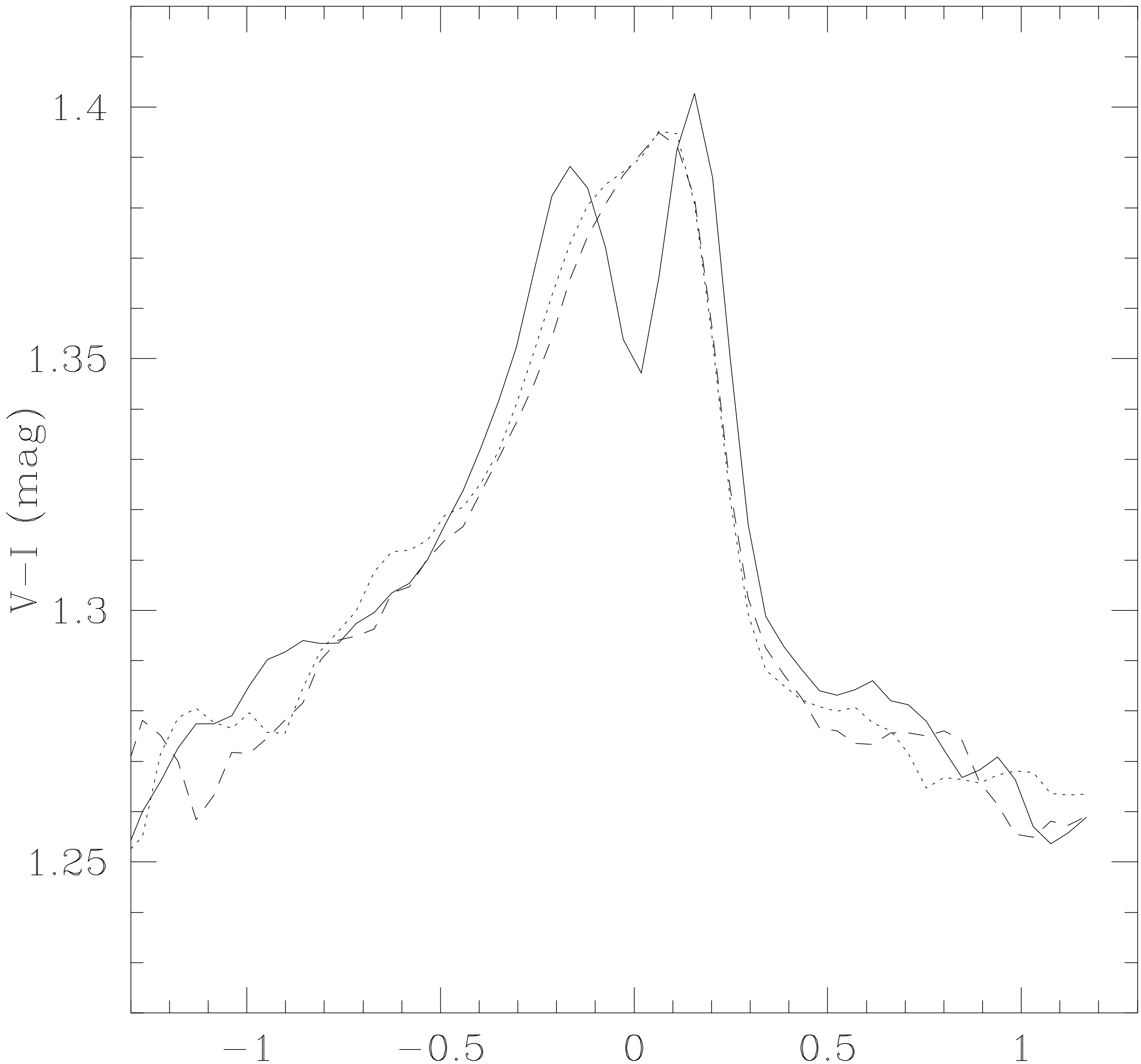
V−I (mag)
1.4
1.35
1.3
1.25
−1
−0.5
0
0.5
1
position (arcsec)

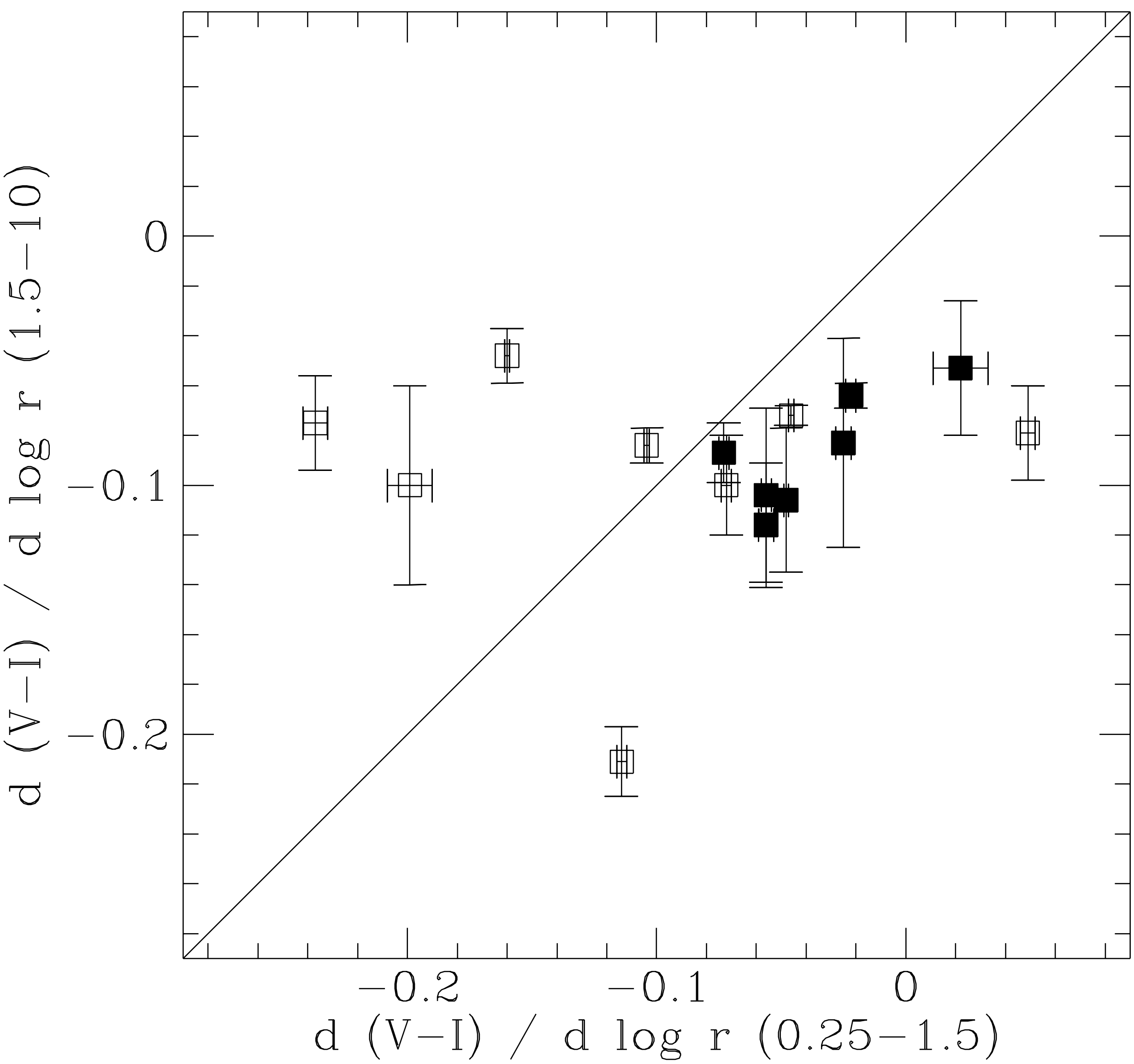
0
−0.1
−0.2
d (V−I) / d log r (1.5−10)
−0.2
−0.1
0
d (V−I) / d log r (0.25−1.5)

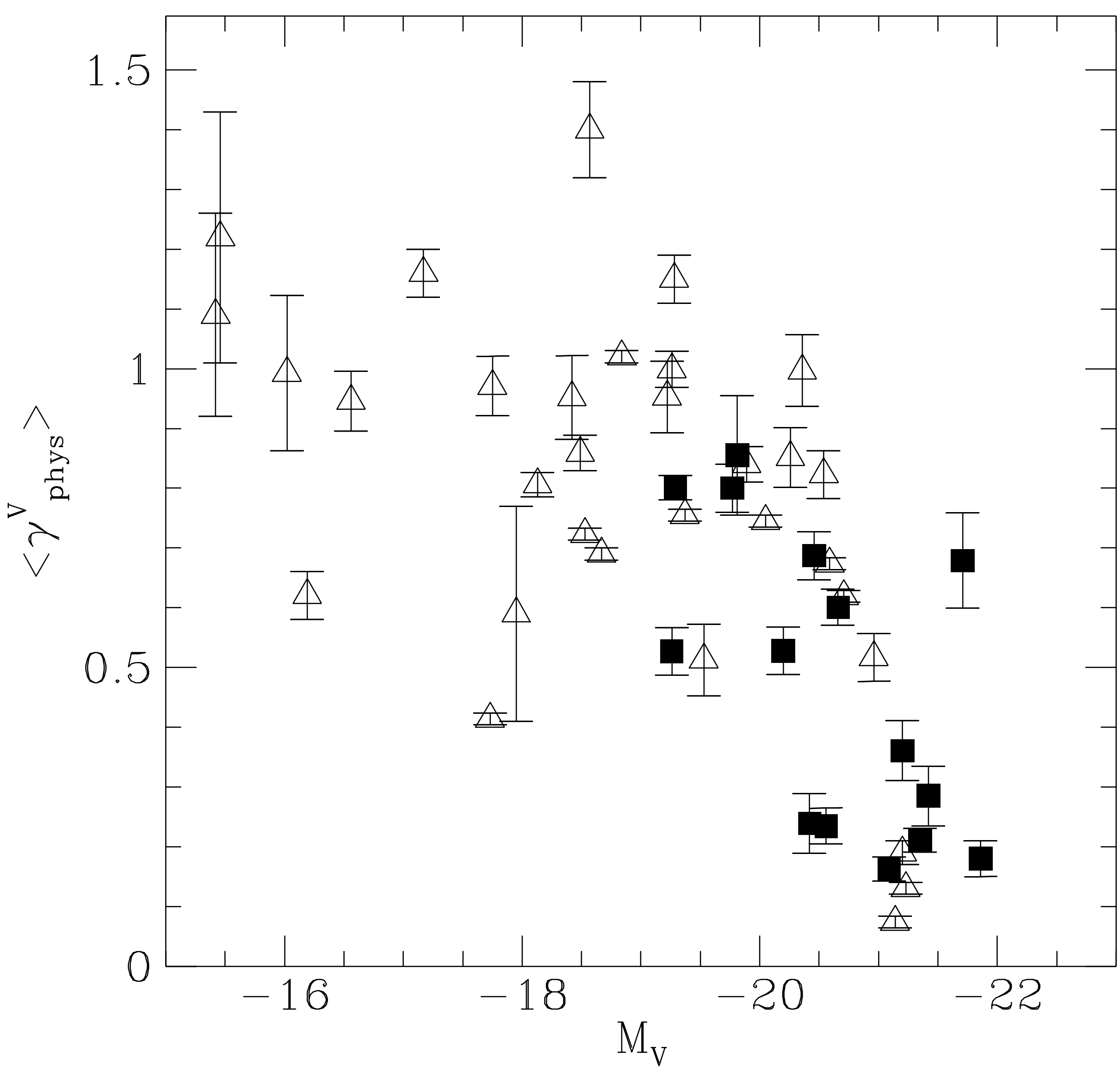

1.5
1
0.5
0
−16
−18
−20
−22
M_V
$<\gamma^V_{phys}>$

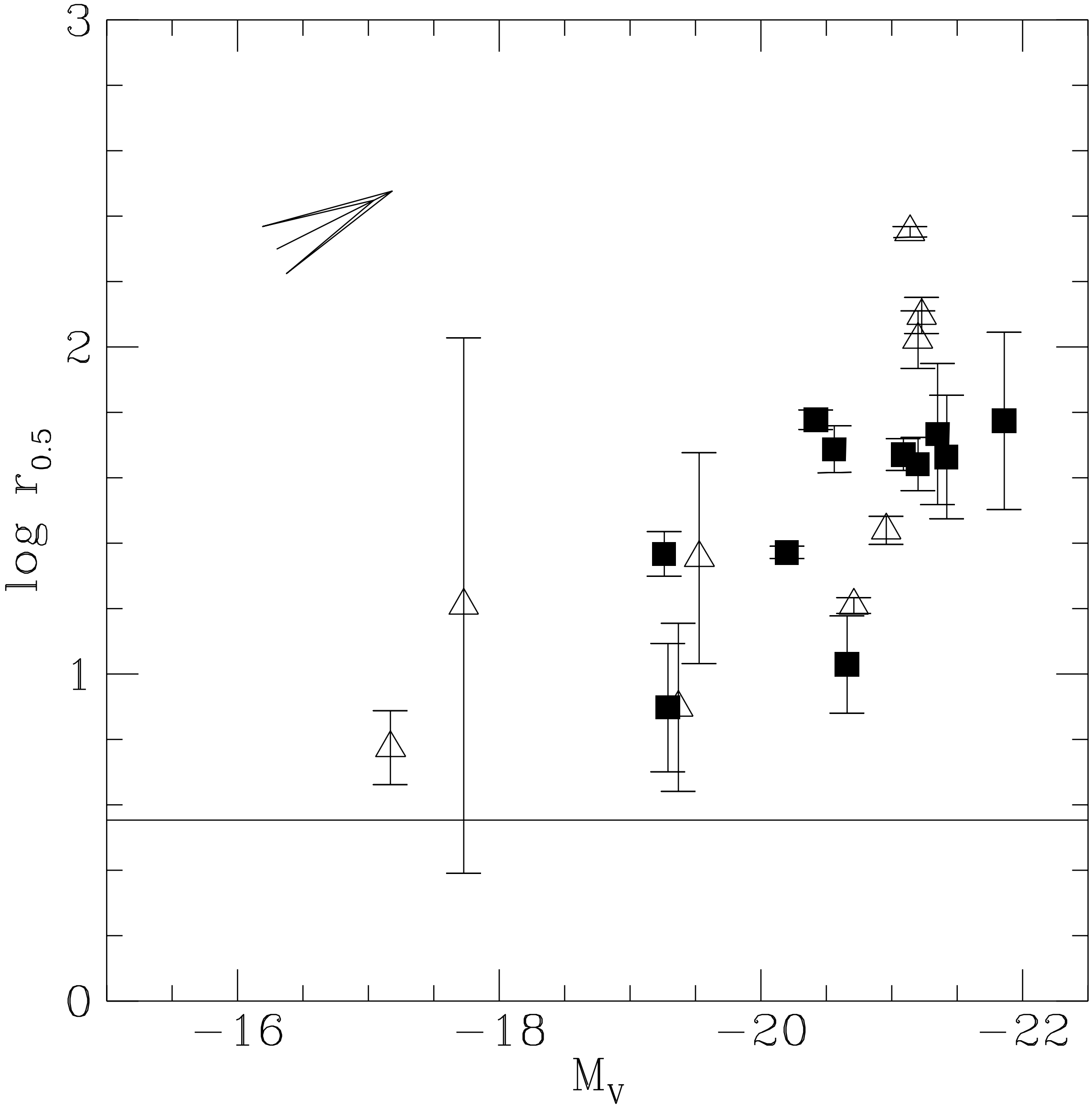

3
2
1
0
log $r_{0.5}$
−16
−18
−20
−22
M_V

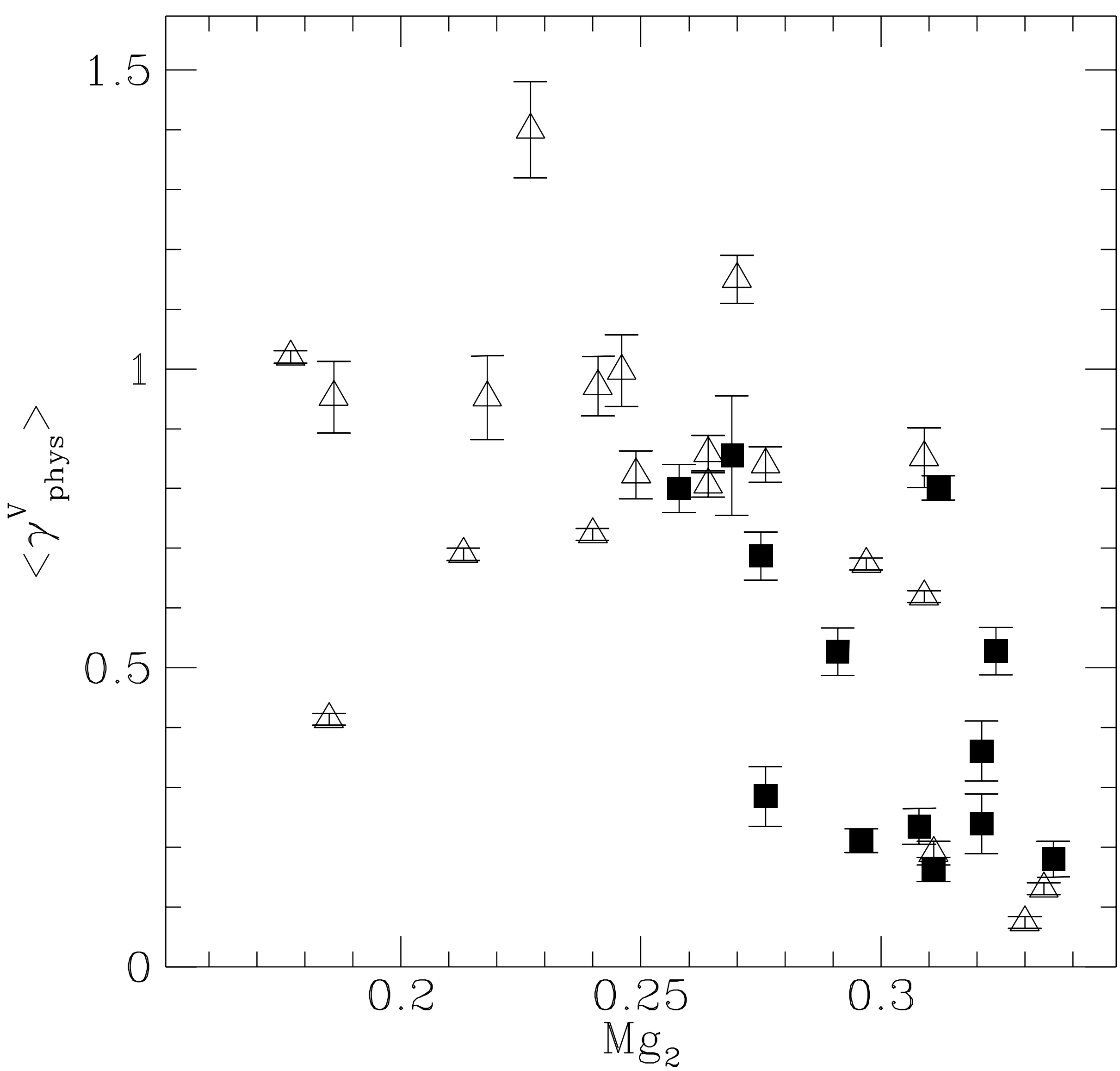
1.5
1
0.5
0
0.2
0.25
0.3
$<\gamma^{V}_{phys}>$
Mg_2

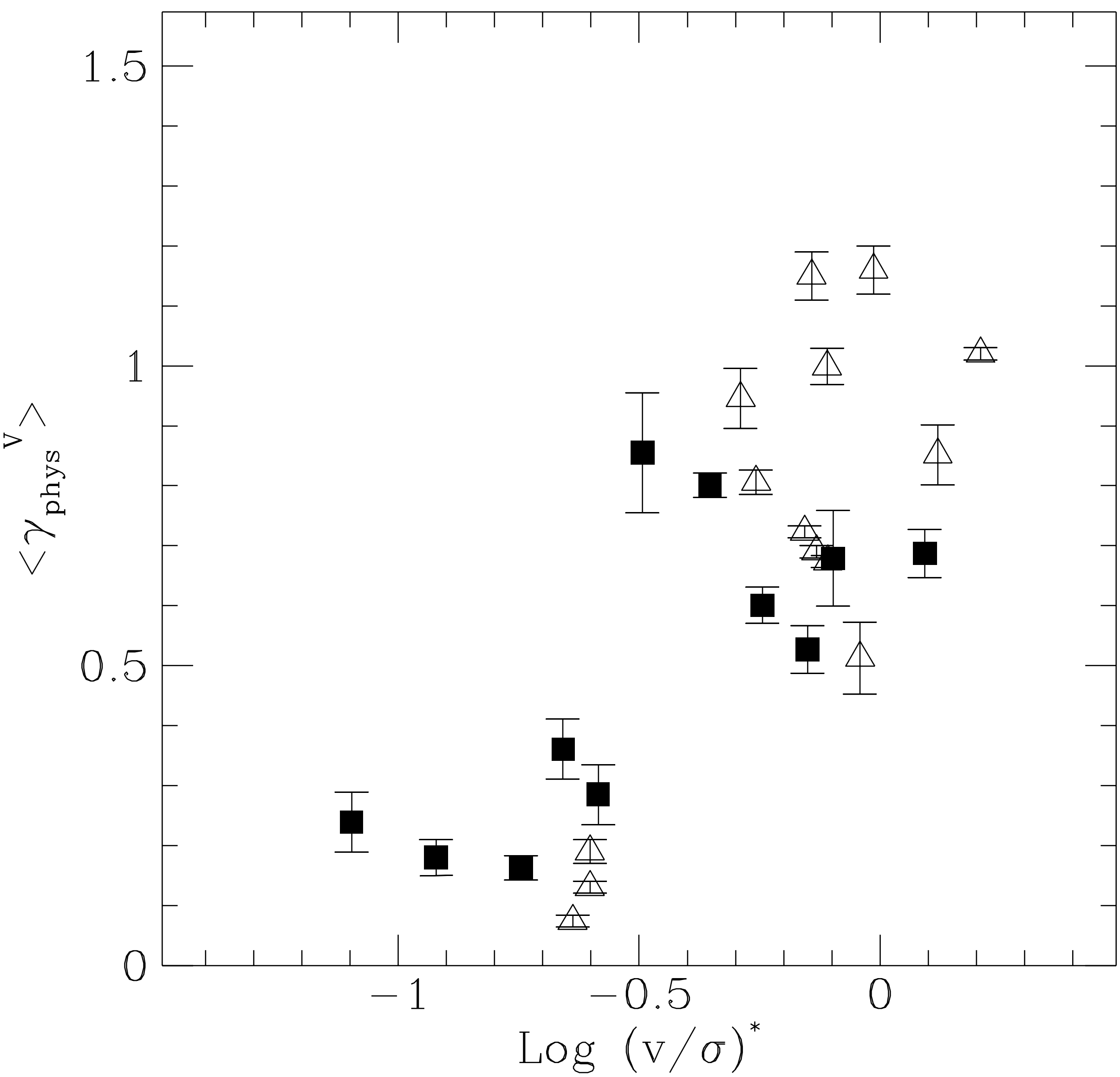

1.5
1
0.5
0
−1
−0.5
0
$\langle \gamma_{\rm phys}^{\rm v} \rangle$
Log $(v/\sigma)^*$

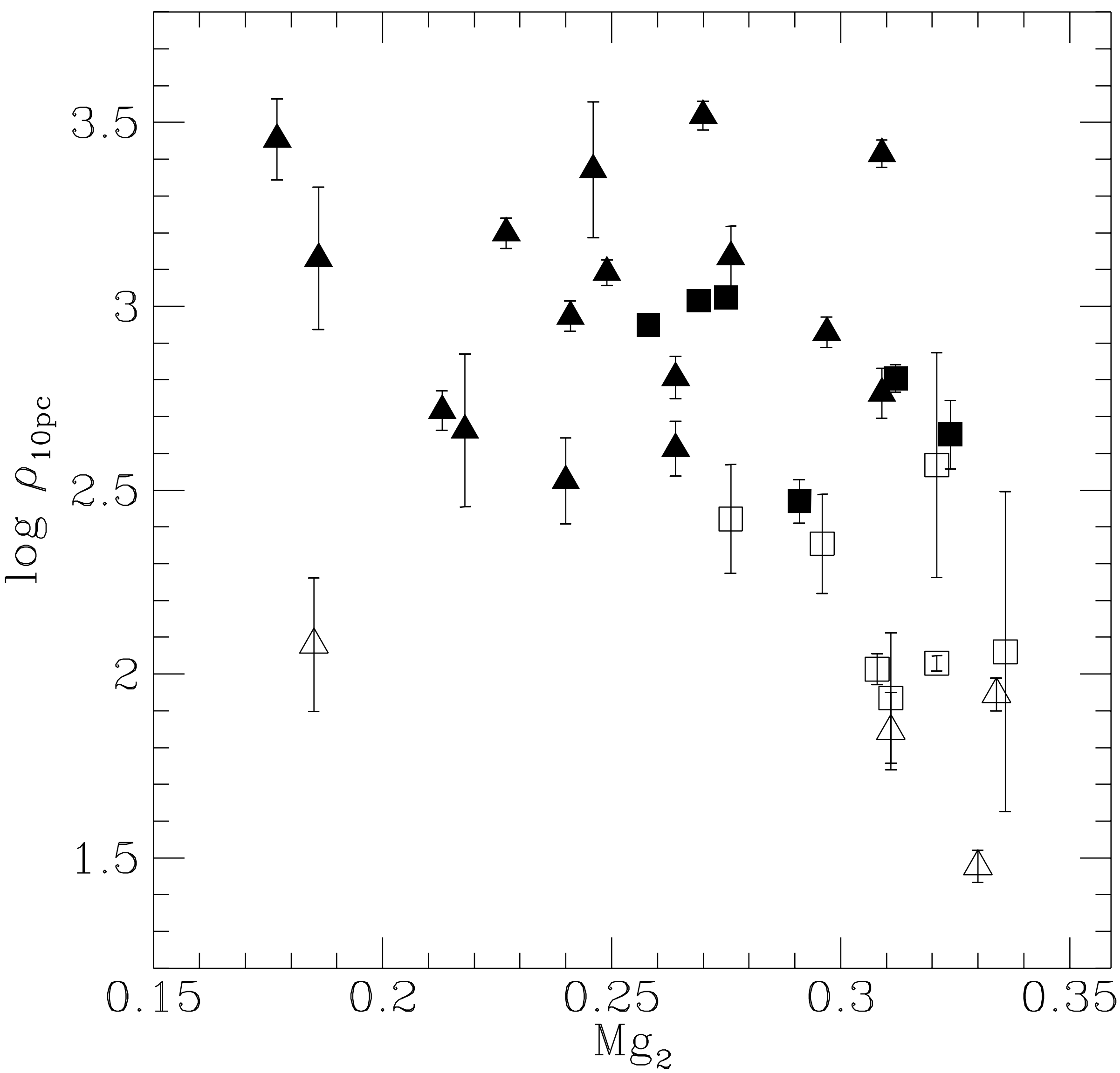

log ρ_{10pc}
3.5
3
2.5
2
1.5
0.15
0.2
0.25
0.3
0.35
Mg_2

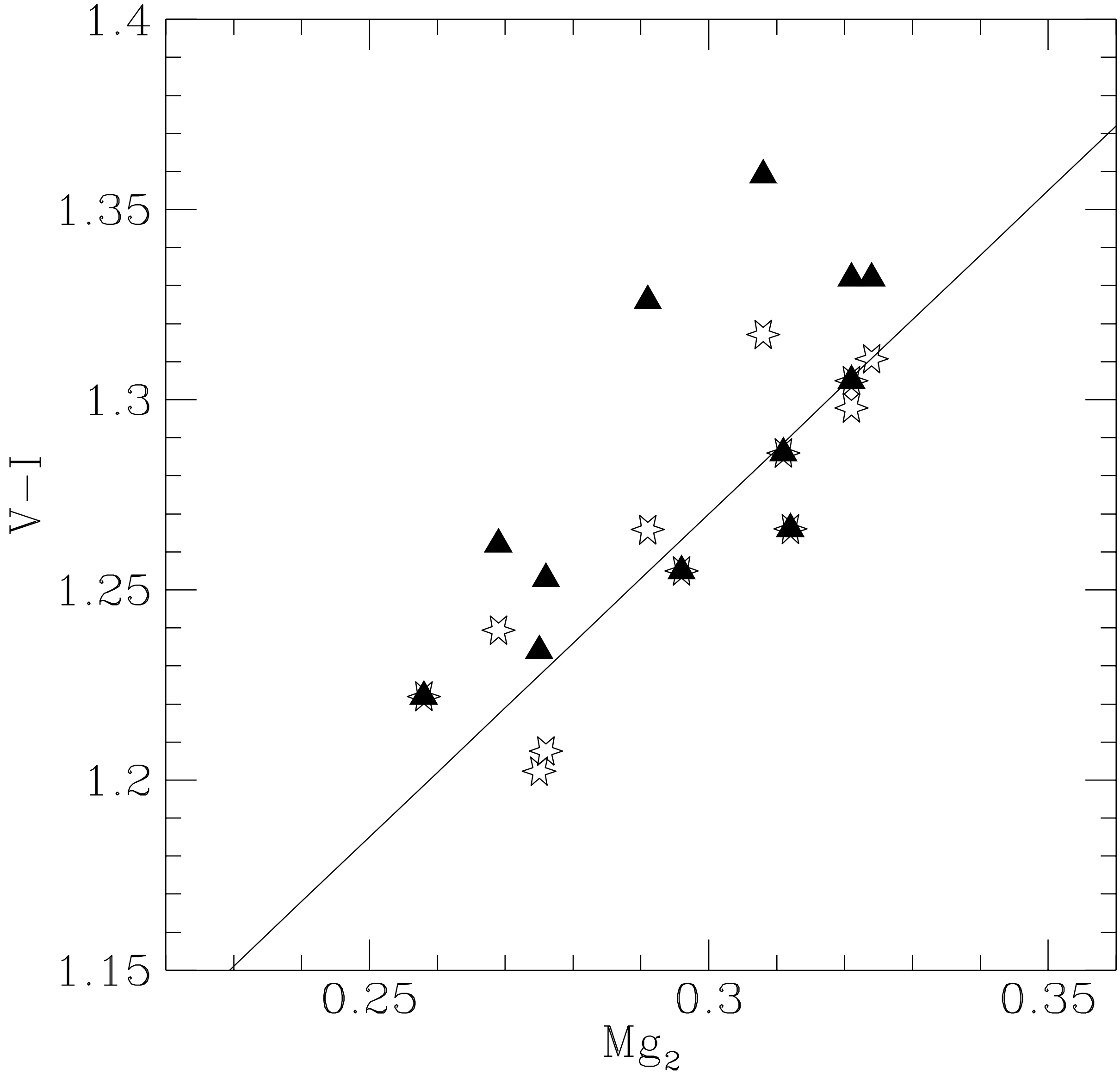
1.4
1.35
1.3
1.25
1.2
1.15
V−I
0.25
0.3
0.35
Mg_2

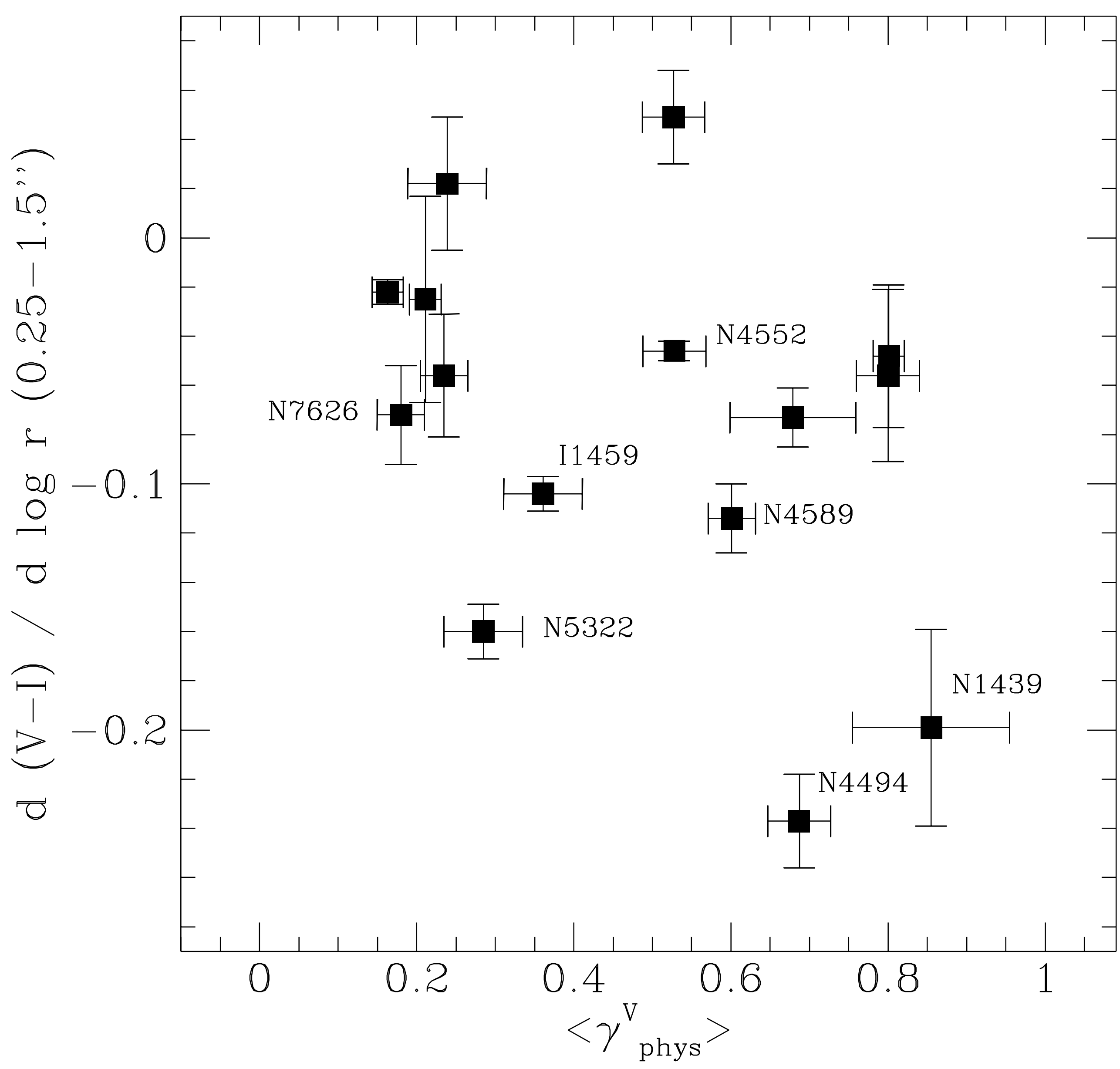
d (V−I) / d log r (0.25−1.5'')
0
−0.1
−0.2
0
0.2
0.4
0.6
0.8
1
<γ^V_phys>
N4552
N7626
I1459
N4589
N5322
N1439
N4494

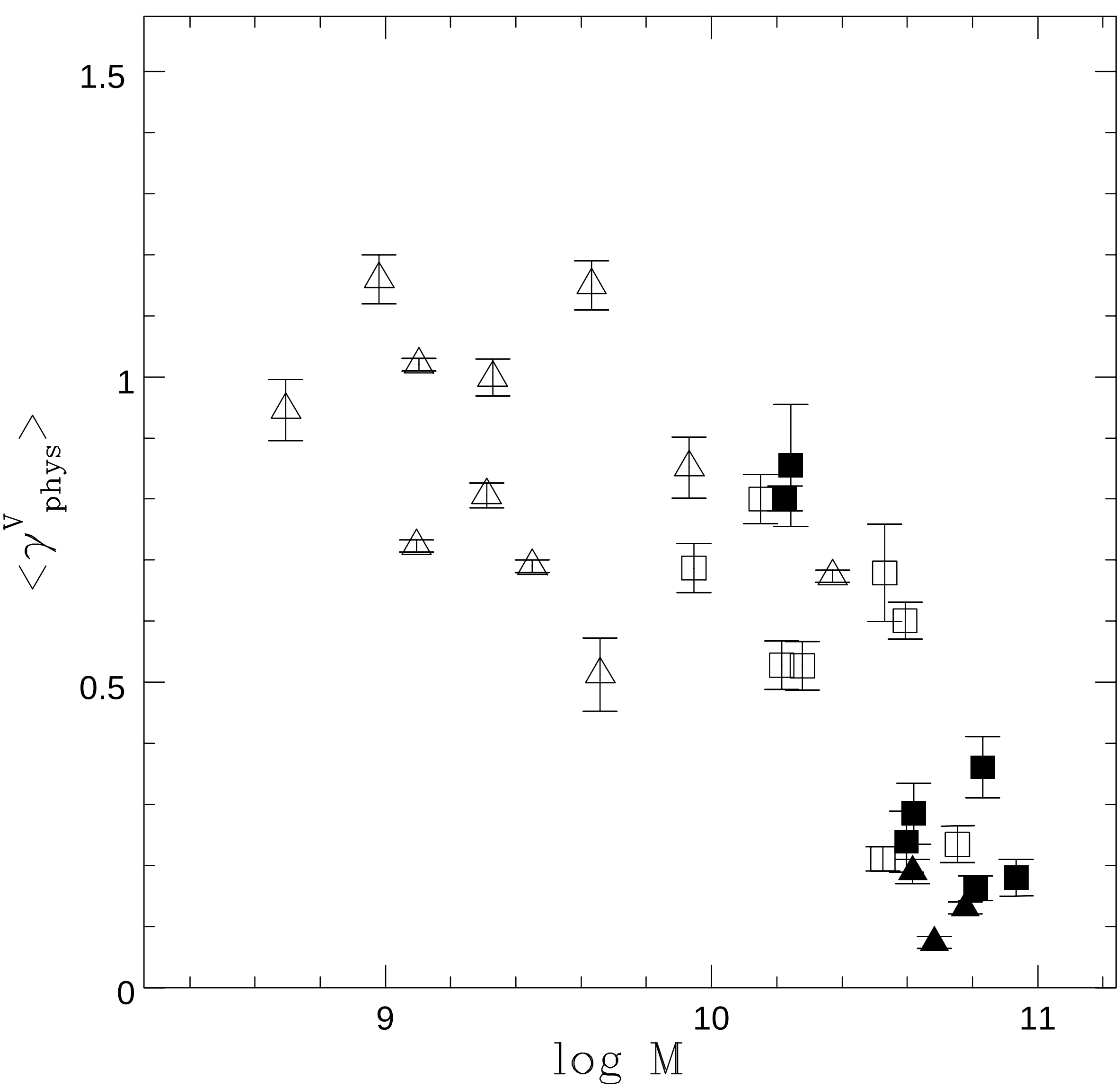

1.5
1
0.5
0
9
10
11
log M
$<\gamma^{V}_{phys}>$

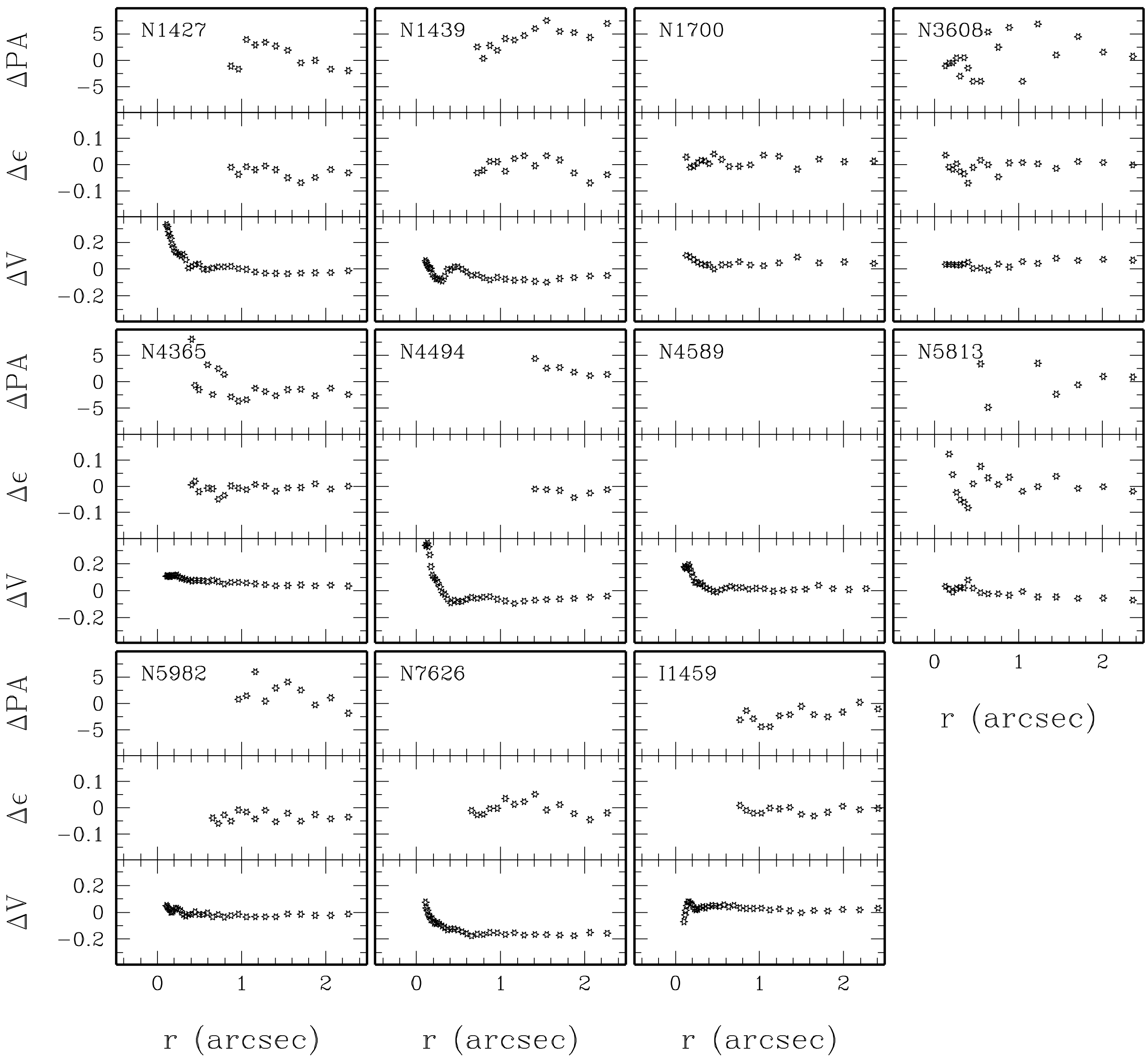

N1427
N1439
N1700
N3608
N4365
N4494
N4589
N5813
N5982
N7626
I1459
ΔPA
Δϵ
ΔV
r (arcsec)

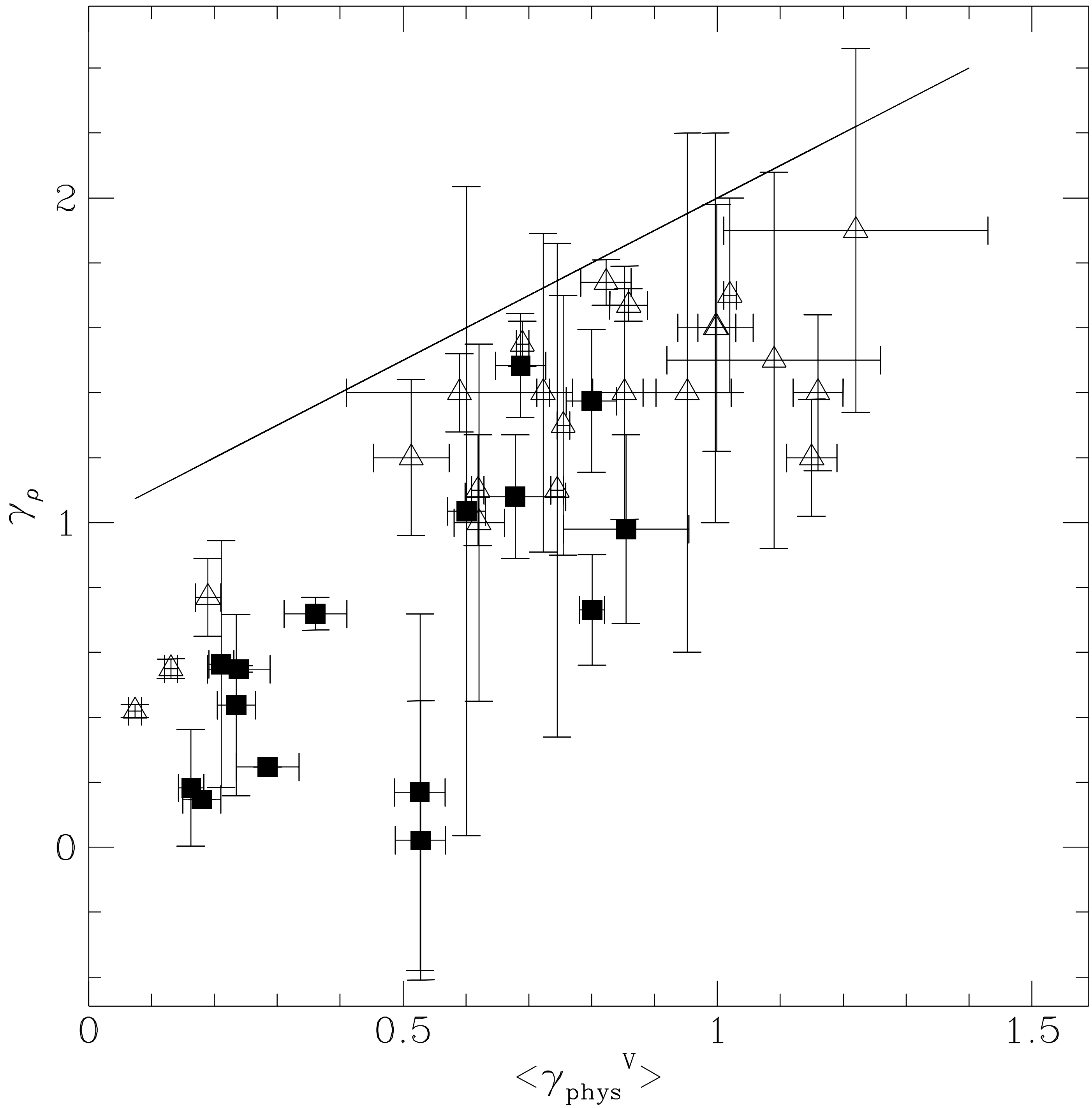

0
1
2
0
0.5
1
1.5
γ_ρ
$<\gamma_{\rm phys}{}^{\rm V}>$

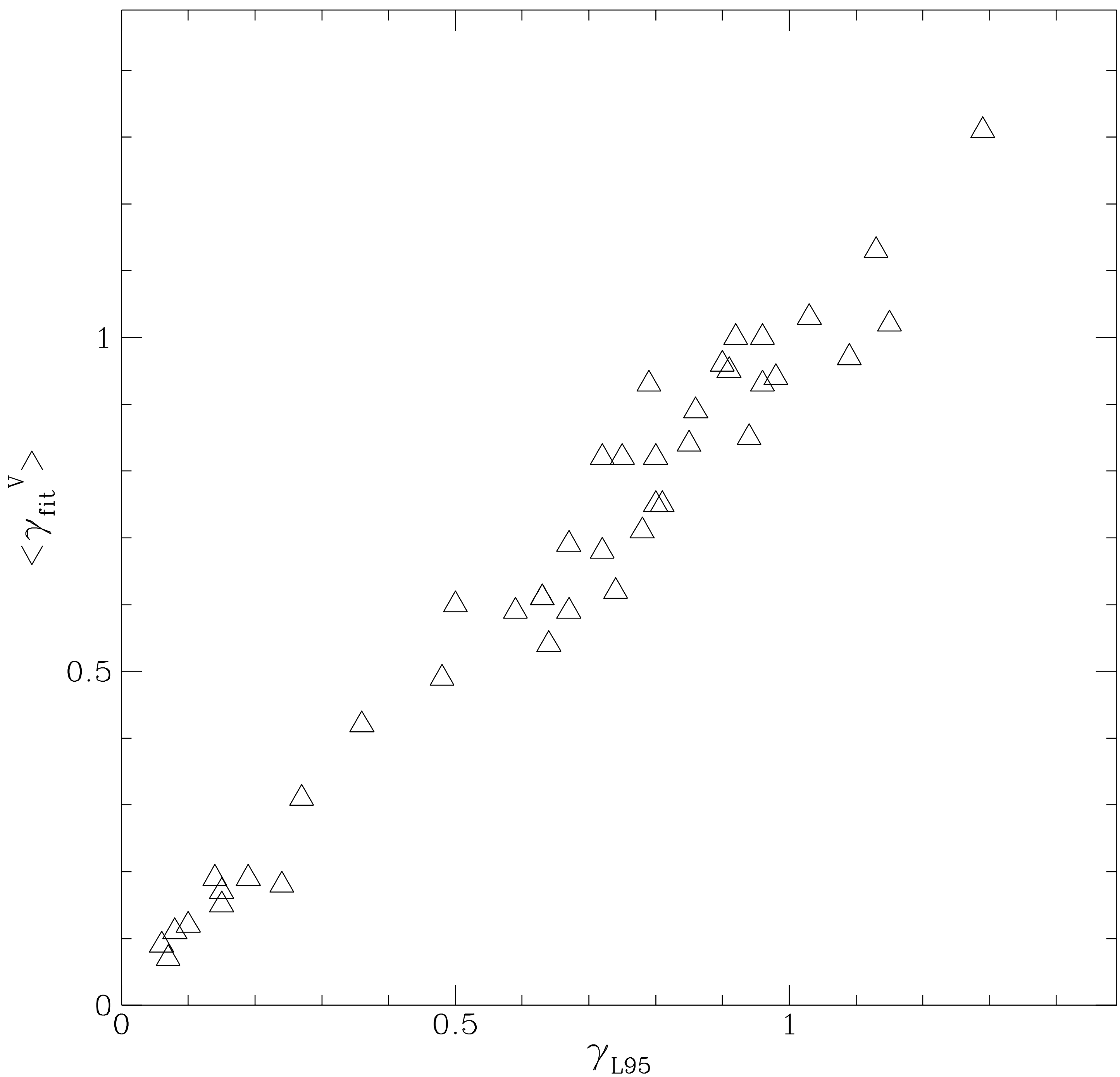

0
0.5
1
0
0.5
1
$\gamma_{\rm L95}$
$<\gamma_{\rm fit}{}^{\rm V}>$

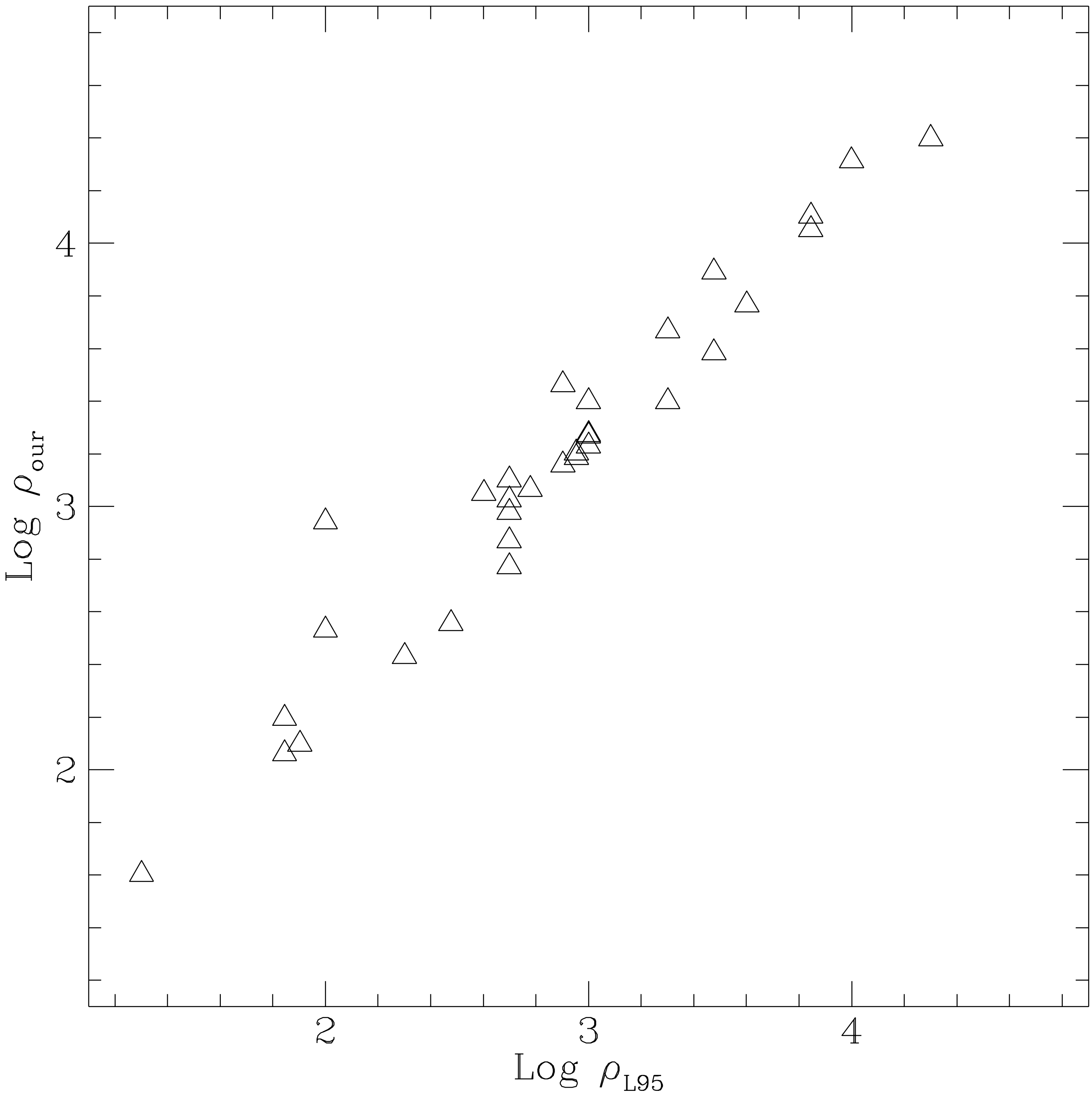

Log $\rho_{\rm our}$
Log $\rho_{\rm L95}$
2
3
4
2
3
4

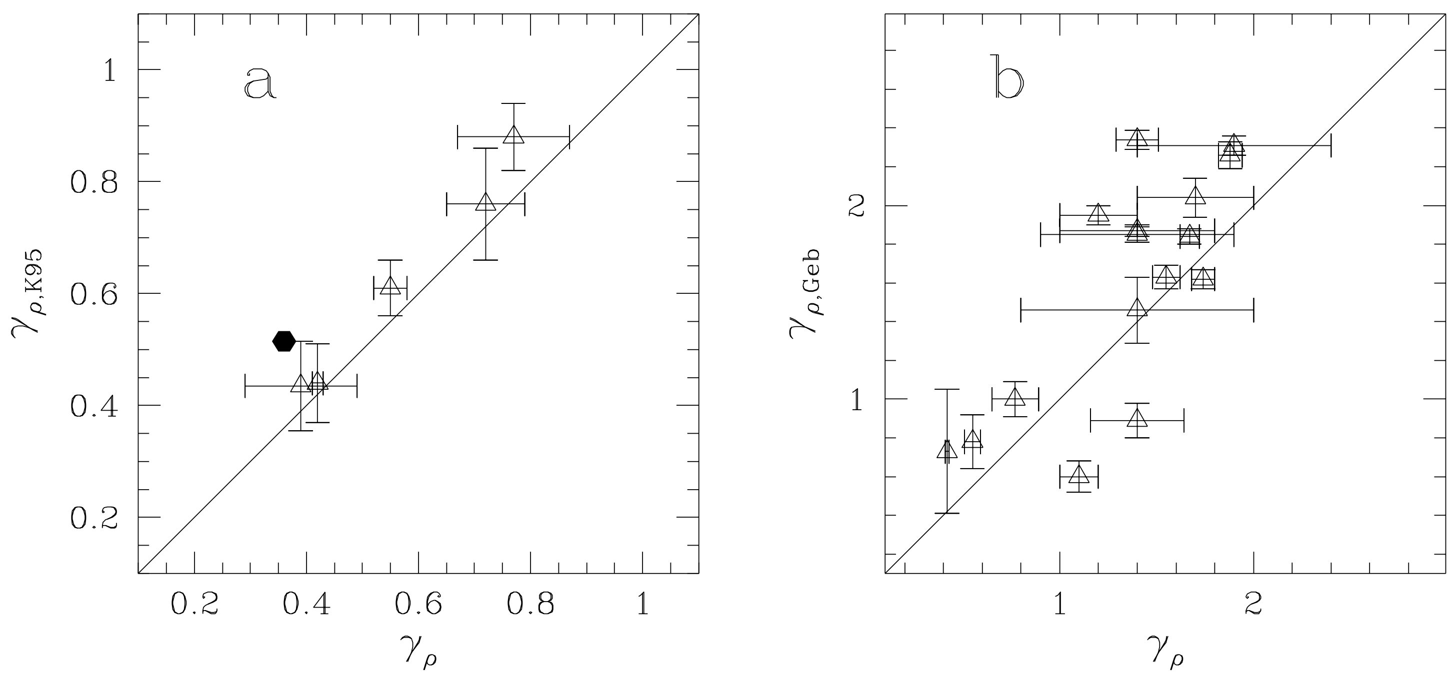

a
b
$\gamma_{\rho,\mathrm{K95}}$
$\gamma_{\rho,\mathrm{Geb}}$
γ_ρ
γ_ρ
0.2
0.4
0.6
0.8
1
1
2